Alexis Balayre

Future Position Prediction for Pressure Refuelling Port of Commercial Aircraft

School of Aerospace, Transport and Manufacturing
Computational and Software Techniques in Engineering

MSc
Academic Year: 2023–2024

Supervisors: Dr Boyu Kuang and Dr Stuart Barnes
May 2024

School of Aerospace, Transport and Manufacturing
Computational and Software Techniques in Engineering

MSc

Academic Year: 2023–2024

Alexis Balayre

Future Position Prediction for Pressure Refuelling Port of Commercial Aircraft

Supervisors: Dr Boyu Kuang and Dr Stuart Barnes
May 2024

This thesis is submitted in partial fulfilment of the requirements for the degree of MSc.

Academic Integrity Declaration

I declare that:

- the thesis submitted has been written by me alone.
- the thesis submitted has not been previously submitted to this university or any other.
- that all content, including primary and/or secondary data, is true to the best of my knowledge.
- that all quotations and references have been duly acknowledged according to the requirements of academic research.

I understand that to knowingly submit work in violation of the above statement will be considered by examiners as academic misconduct.

Abstract

This thesis presents the development of a robust and efficient framework for predicting the future position of the pressure refuelling port of commercial aircraft. The proposed framework addresses critical challenges in automated aircraft refuelling systems, where accurate detection and prediction of the refuelling port's position is essential for operational efficiency and safety. Leveraging deep learning techniques, the framework integrates a fine-tuned YOLOv10 object detection model with a novel sequence prediction model, termed SizPos-GRU. This sequence model utilizes an encoder-attention-decoder architecture to effectively capture temporal dependencies and spatial relationships from video frames. The methodology includes meticulous dataset configuration and annotation, followed by hyperparameter tuning to optimize model performance. Experimental results demonstrate the SizPos-GRU model's superior predictive accuracy across different scenarios, validated through metrics such as Average Displacement Error (ADE), Final Displacement Error (FDE), and Intersection over Union (IoU). The implementation of smoothing filters like Savitzky-Golay and the application of Extended Kalman Filters further enhance the prediction stability and reliability. The research findings highlight the potential of the proposed framework to significantly improve the automation of aircraft ground operations, making a valuable contribution to the field by advancing the state-of-the-art in predictive modeling for dynamic environments.

Keywords:
Automated aircraft refuelling, Object detection, Deep learning, YOLOv10, SizPos-GRU, Spatio-temporal prediction, Kalman filtering, Savitzky-Golay smoothing

Acknowledgements

I would like to express my deepest gratitude to my supervisors, Dr. Boyu Kuang and Dr. Stuart Barnes, for their invaluable guidance, encouragement, and support throughout this research. I am especially grateful to Dr. Boyu Kuang, whose unwavering dedication, insightful feedback, and willingness to go the extra mile have been instrumental in overcoming the challenges faced during this study. His mentorship has not only greatly enriched the quality of this thesis but also inspired me to pursue excellence in my research. I would also like to extend my appreciation to the faculty and staff of the School of Aerospace, Transport and Manufacturing at Cranfield University for providing an enriching academic environment and the necessary resources to carry out this research. Special thanks to my colleagues and fellow students for their camaraderie and for sharing ideas that have contributed to the development of this work. I am deeply grateful to my family and friends for their unwavering support and understanding during the course of my studies. Their belief in me has been a source of strength and motivation. Finally, I would like to acknowledge the financial support provided by UKRI through the ONEHeart project, which made this research possible. The data and resources provided through this project have been essential to the completion of this thesis.

Table of Contents

List of Figures

List of Tables

List of Abbreviations

ML	Machine Learning
DL	Deep Learning
AI	Artificial Intelligence
CNN	Convolutional Neural Network
RNN	Recurrent Neural Network
LSTM	Long Short-Term Memory
GRU	Gated Recurrent Unit
EKF	Extended Kalman Filter
AAGR	Autonomous Aircraft Ground Refueling
AGR	Aircraft Ground Refueling
UAV	Unmanned Aerial Vehicle
AAR	Autonomous Aerial Refueling
DGPS	Differential Global Positioning System
SVM	Support Vector Machine
HOG	Histogram of Oriented Gradients
SOTA	State-of-the-Art
AIS	Automatic Identification System
GPS	Global Positioning System
IoU	Intersection over Union
TP	True Positive
FP	False Positive
FN	False Negative
TN	True Negative
AP	Average Precision
AR	Average Recall
SSD	Single Shot Multibox Detector
YOLO	You Only Look Once
IoT	Internet of Things
AFRL	Air Force Research Laboratory
AR3P	Autonomous & Robotic Remote Refueling Point
BIPRS	Brightness Invariant Port Recognition System

Chapter 1

Introduction

1.1 Background and Motivation

Ground pressure refuelling is a standard method used to refuel commercial aircraft safely and efficiently. This process involves using a system of underground fuel pipelines and hydrants at aircraft parking spots [6]. When an aircraft is ready for refueling, a hydrant dispenser vehicle connects to the hydrant pit and delivers fuel to the aircraft through a flexible hose [42] (see Figure 1.1). This method allows for high fuel flow rates and significantly reduces aircraft turnaround times [6]. However, this process also presents several challenges, particularly in terms of safety and accuracy. In the past, there have been several incidents involving ground pressure refueling, including fuel spills, overfills, and equipment failures [37, 13]. Fortunately, with the advancement of technology, many of these challenges will be addressed, and the refueling process will become safer and more efficient.

Figure 1.1: Pressure Refuelling of a Commercial Aircraft. Photo Credit: Tom Boon/Simple Flying [4]

The aviation industry is undergoing a significant transformation with the development of the airport of the future, commonly known as 'Smart Airport' or, more recently, 'Airport 4.0'. The concept of Smart Airport encompasses the use of cutting-edge information technologies, such as the Internet of Things (IoT), Artificial Intelligence (AI), and Blockchain, to monitor, analyse, and integrate real-time data on the airport's status. This integration aims to achieve optimal operational efficiency and enhance the quality of service. Taking the concept a step further, Airport 4.0 envisages an airport driven entirely by AI, capable of making autonomous decisions thanks to self-learning mechanisms. This advance aims to automatically predict and

manage various airport scenarios, making it easier to automate numerous processes. The result is a substantial reduction in operating costs and error rates [34].

Among these, automated refuelling systems play a crucial role in ensuring efficient and accurate refuelling of aircraft. However, one of the main challenges of this automation process is the accurate detection of the aircraft's refuelling port, which is relatively small and can easily be obscured by other visual elements on or near an aircraft. For example in the Figure 1.2, the refuelling port is located on the wing of the aircraft and can be difficult to detect due to motion blur, occlusion, or being out of view. This challenge is further compounded by the fact that aircraft refuelling ports can vary in size, shape, and location depending on the aircraft type and manufacturer. Scanning the entire area of each video frame is both time-consuming and inaccurate. It is therefore essential to develop a more efficient and accurate method of locating the refuelling port.

(a) Motion Blur Example (b) Occlusion Example (c) Out-of-View Example

Figure 1.2: Challenges in Detecting Aircraft Refuelling Port

1.2 Research Gap

Despite significant advancements in autonomous aircraft ground refuelling technologies, critical challenges remain, particularly in the accurate detection and positioning of the refuelling port. The small size and varied locations of refuelling ports, often obscured by visual elements like motion blur and occlusions, complicate this task. Existing systems have made progress using machine vision, but they are limited by inefficiencies in scanning entire video frames and inaccuracies under different environmental conditions. Furthermore, while current methodologies leveraging convolutional neural networks (CNNs) and Kalman filters have improved detection accuracy, they still struggle with real-time performance and adaptability in dynamic environments. The robustness of these systems in varied lighting conditions and their capability to handle different refuelling port types and obstructions need enhancement. Additionally, the application of advanced deep learning models like Long Short-Term Memory (LSTM) networks, Recurrent Neural Networks (RNNs), and Transformers in this context is underexplored.

1.3 Aim and Objectives

This thesis aims to address the previous research gaps by developing a framework for predicting the future position of commercial aircraft refuelling ports using advanced Object Detection models and Deep Learning to leverage the spatial-temporal relationship between frames in a video.

1. Conduct a comprehensive review of state-of-the-art methods for Object Detection, Object Tracking, and Deep Learning Sequence Models.

2. Annotate and preprocess video datasets of aircraft refuelling ports to ensure high-quality training and testing data.

3. Design and develop a framework for accurately tracking and predicting the future position of aircraft refuelling ports.

1.4 Technological Contributions

This thesis makes several technological contributions aimed at advancing the field of automated aircraft refuelling systems. The primary contribution is the integration of advanced deep learning models, including Long Short-Term Memory (LSTM) networks and Gated Recurrent Unit (GRU) networks, to predict the future positions of refuelling ports by leveraging their superior spatio-temporal data processing capabilities. Another significant contribution is the development of an innovative framework that combines object detection, target tracking, and future position prediction to enhance the accuracy and efficiency of automated refuelling systems. This framework is designed to handle the small pixel ratio of refuelling ports efficiently, thus optimising the detection and tracking process. The use of Extended Kalman Filtering (EKF) further refines predictions, ensuring real-time adaptability and accuracy, which is crucial for practical applications in busy airport environments.

1.5 Thesis Layout

The following sections of this thesis provide a detailed exploration and analysis of the methodologies, experiments, and findings related to the development of an advanced framework for predicting the future positions of aircraft refuelling ports. The Chapter 2 (Literature Review) presents an overview of the current state-of-the-art methods in automated aircraft refuelling systems, object detection, and deep learning for spatio-temporal prediction. The Chapter 3 (Methodology) describes the step-by-step approach taken in dataset preparation, framework design, and model training. The Chapter 4 (Experiment Design) outlines the experimental setups and comparison studies conducted to evaluate the performance of the proposed models. In the Chapter 5 (Results and Discussion), the outcomes of these experiments are presented and analysed, offering insights into the effectiveness and implications of the research findings. Finally, the Chapter 6 (Conclusion and Future Work) summarises the key contributions of the thesis, reflects on the significance of the results, and proposes directions for future research to further advance the field of automated aircraft refuelling systems.

Chapter 2

Literature Review

2.1 Automated Refulling Systems in the Aviation Industry

Ground refueling operations are essential to maintaining aircraft availability and operational efficiency. The transition from manual to automated systems is designed to improve the safety, efficiency and reliability of these operations [38]. The concept of Autonomous Aircraft Ground Refueling (AAGR) emerged in the 1980s in the United States to address the US Air Force's need to protect ground personnel from potential threats during refueling operations [43]. In the early 1990s, Bennett et al. [5] introduced the Brightness Invariant Port Recognition System (BIPRS), marking a significant advancement in machine vision systems for identifying aircraft refuelling ports. In 2010, the Air Force Research Laboratory (AFRL) showcased the world's first Automated Aircraft Ground Refuelling system prototype through a video demonstration. This system featured a robot equipped with a fuel nozzle and a single-point refuelling adapter, enabling autonomous engagement with the aircraft's refuelling panel, as illustrated in Figure 2.1 [9]. This project will give birth to the Autonomous & Robotic Remote Refuelling Point (AR3P) project.

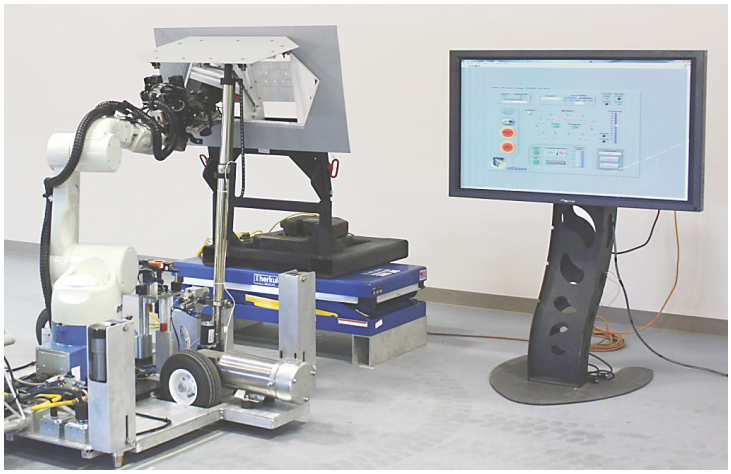

Figure 2.1: AFRL's Automated Aircraft Ground Refueling system prototype robot (Photo Credit: AFRL/RXQ Robotics Group)

The Autonomous & Robotic Remote Refuelling Point (AR3P) project, developed by the U.S. Army, represents a pioneering initiative in unmanned refuelling operations for rotary-wing aircraft. This project leverages advanced robotics, including self-aligning mechanisms

and articulated arms equipped with sensors, to facilitate rapid and safe refuelling processes on non-contiguous battlefields. The AR3P system minimises the time aircraft spend on the ground and enhances safety by reducing soldier exposure at fueling stations. Initially demonstrated in a Limited Initial Capabilities event, the AR3P aims to meet the evolving range and endurance requirements of Army Aviation. The project integrates existing technologies with novel systems designed in-house, supported by commercial off-the-shelf components and additive manufacturing. Currently, AR3P is progressing through its development phases, addressing technical risks, and preparing for further testing and eventual deployment, as shown in Figure 2.2 [17].

Figure 2.2: AR3P Concept Development Prototype Robot (Photo Credit: U.S. Army)

The AR3P project exemplifies the intersection of advanced robotics and practical military applications, highlighting the potential of automated systems to transform operational paradigms. Figure 2.3 provides visual insights into the capabilities of the AR3P system, by performing autonomous hot refuelling. During this test, the robot is equipped with a LIDAR sensor and a camera to detect the aircraft's refuelling port. In Figure 2.3a, the AR3P robot is seen approaching a detected aircraft, demonstrating its autonomous navigation and alignment capabilities. In Figure 2.3b, the AR3P robot is shown engaging the aircraft refuelling port, emphasising its precision and functionality in connecting to the aircraft's fuel port. These images illustrate the practical implementation of robotic technologies in enhancing the safety, efficiency, and speed of refuelling operations, particularly in challenging and hazardous environments [3].

(a) AR3P Robot Approaching Detected Aircraft (Photo Credit: Stratom)

(b) AR3P Robot Engaging Aircraft Refueling Port (Photo Credit: Stratom)

Figure 2.3: AR3P Robot Hot Refueling Demonstration for S-70 Helicopter

Unfortunately, there is very little literature on existing AAGR systems, as most research is carried out by the military and is classified. The most recent papers cover Autonomous Aerial Refueling (AAR) systems, which are used to refuel unmanned aerial vehicles (UAVs) in mid-air. These systems are designed to extend the flight time and range of UAVs by enabling them to refuel without landing. AAR systems are particularly challenging due to the high speeds and altitudes involved, as well as the need for precise measurement and tracking of the relative position between the receiver aircraft and the tanker aircraft are critical, particularly during the docking phase (see figure 2.4) [22, 48]. Zhong et al. [57] propose a robust solution that utilises monocular vision combined with an extended Kalman filter (EKF) to address this challenge. By implementing EKF, the system can provide reliable position estimations and track the drogue within a specified region of interest (ROI), even in the presence of disturbances such as air turbulence. As shown in figure 2.5, this system initialises the state and covariance matrices, predicts the drogue's position, updates the state based on new measurements, and continuously refines the ROI for subsequent image processing. This approach significantly reduces the processing time and improves the detection frequency from 10 Hz to up to 30 Hz by focusing computational resources on the predicted ROI.

Figure 2.4: Autonomous Aerial Refueling (AAR) of X-47B Unmanned Combat Air System Demonstrator (Photo Credit: U.S. Navy)

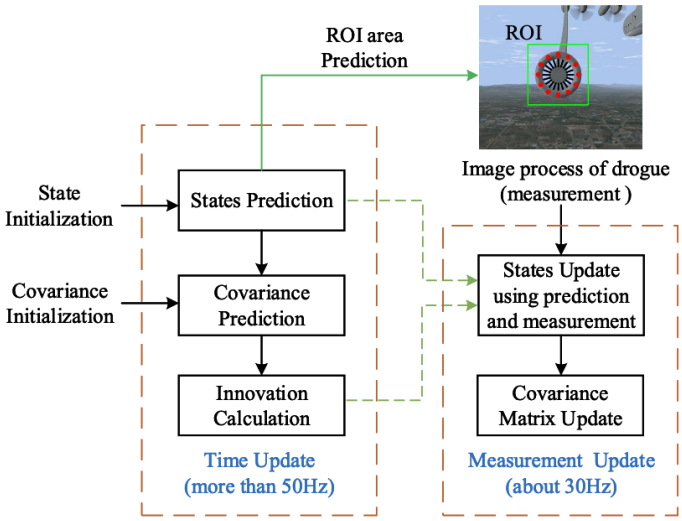

Figure 2.5: Autonomous Air Refueling Detection System with EKF. Source: Zhong et al. [57]

Recent advancements in autonomous ground refuelling have been driven by improvements in computer vision and robotics. Yildirim et al. [53] presented the PosEst system, which combines 2D RGB images with 3D point cloud data to enhance detection accuracy. This system uses a custom-trained EfficientNet-B0 CNN for object detection and leverages the Kalman filter for stable 3D pose estimation (see Figure 2.6). The PosEst method employs a dual approach of high-precision detection and robust tracking. By predicting and updating the object's state in real-time, the Kalman filter facilitates continuous and precise alignment of the fuel nozzle with the refuelling adaptor, even in dynamic environments. This approach significantly reduces the risks associated with manual refuelling and improves operational efficiency and safety.

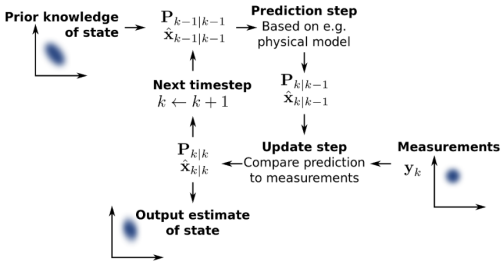

Figure 2.6: Kalman Filter Workflow for Pose Estimation in Autonomous Ground Refueling. Source: Yildirim et al. [53]

One of the primary challenges in AAGR is the accurate detection and positioning of the refuelling port under varying environmental conditions. Robust datasets for scene recognition and machine learning applications have been developed to address these challenges. Kuang et al. [29] introduced a comprehensive dataset for AAGR, addressing significant challenges such as variant illumination conditions, different refuelling port types, and environmental obstructions. The dataset comprises over 26,000 labeled images collected through image crawling from 13 different databases, followed by augmentation to ensure diversity (see Figure 2.7). Additionally, recent innovations have introduced hybrid datasets combining real and synthetic data for training and validating systems [54]. This approach offers a wide range of scenarios and conditions, improving the robustness and accuracy of automated refuelling systems. The development of high-quality datasets is pivotal in improving the robustness and reliability of AAGR systems.

Figure 2.7: AAGR Dataset Overview. Source: Kuang et al. [29]

2.2 Object Detection and Tracking in Computer Vision

In Computer Vision, Object Detection refers to the identification and location of individual objects within an image, providing both spatial information (bounding boxes) and confidence scores, which represent the probability that each detected object belongs to the predicted class [15]. For example, in the following image, there are five detections, including one 'ball' with a confidence level of 98% and four 'people' with confidence levels of 98%, 95%, 97% and 97%.

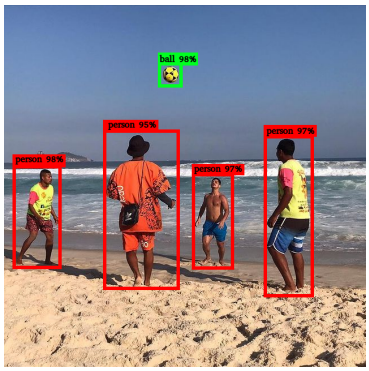

Figure 2.8: Example of outputs from an object detector [15].

Over the last few decades, Object Detection models based on Deep Learning have enjoyed remarkable success. These models fall into two main categories: two-stage detectors and single-stage detectors. On the one hand, two-stage detectors, such as R-CNN [21], Fast R-CNN [20], Faster R-CNN [41] and R-FCN [14], first generate region proposals and then refine these proposals into precise anchor boxes. While these models excel in detection accuracy, they typically suffer from large model sizes and slower detection speeds [27, 52]. On the other hand, single-stage detectors, including the SSD (Single Shot Multibox Detector) [36], YOLO (You Only Look Once) series [40, 39, 7, 11, 18, 24, 32, 25, 47, 50, 46, 51, 45], and RetinaNet [33] directly predict object locations and categories in a single network pass. These models are known for their high detection speeds but sometimes compromise accuracy [27, 52].

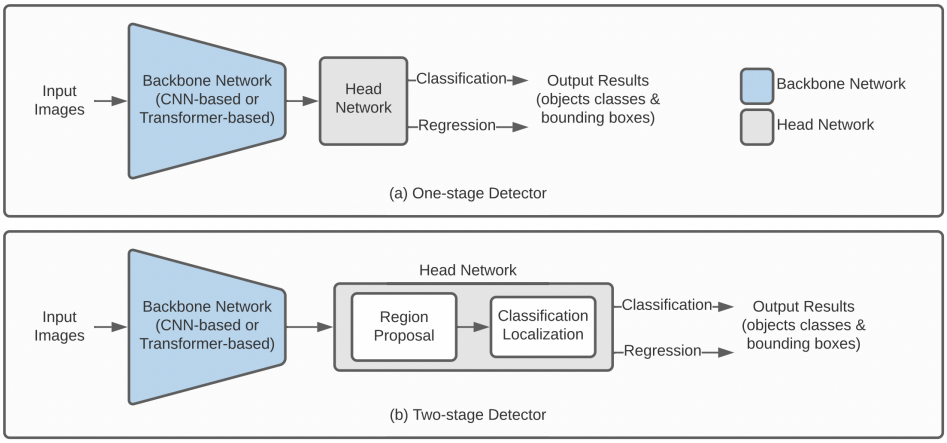

Figure 2.9: Basic deep learning-based one-stage vs two-stage object detection model architectures [27].

YOLOv10, the latest iteration in the YOLO series, marks a significant leap forward in real-time object detection with the introduction of NMS-free training. Traditionally, single-stage detectors relied on Non-Maximum Suppression (NMS) during post-processing to eliminate redundant predictions, as illustrated in Figure 2.10. However, this process can sometimes be overly aggressive, risking the loss of valuable predictions or failing to remove all duplicates effectively, which also adds to computational costs during both training and inference [19].

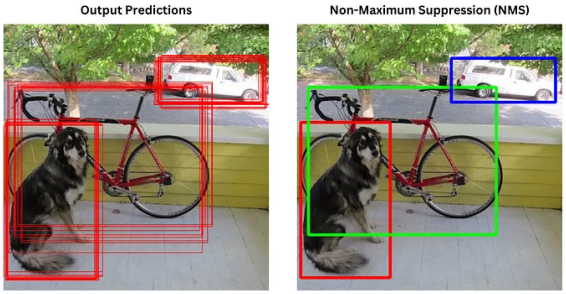

Figure 2.10: Non-Maximum Suppression (NMS) in Object Detection [19].

YOLOv10 overcomes these limitations by implementing a consistent dual assignments strategy that facilitates NMS-free training. This strategy leverages both one-to-many and one-to-one label assignments during training, providing the model with rich supervision while enabling efficient end-to-end deployment. During inference, the one-to-one assignment head is employed, which eliminates the need for NMS and significantly reduces inference time. As depicted in Figure 2.11, the one-to-many head assigns multiple labels to each anchor box, enriching the model's supervision, while the one-to-one head refines these predictions by assigning a single label to each anchor box, ensuring precise and efficient detection [45].

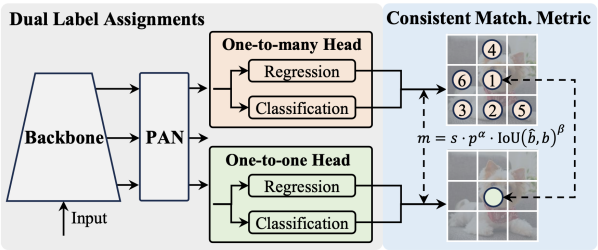

Figure 2.11: YOLOv10 Model Workflow [45]

In addition, YOLOv10 adopts a holistic efficiency-accuracy driven design that optimises the model's architecture across various dimensions. The classification head has been redesigned to be more lightweight, reducing computational overhead while maintaining accuracy. The spatial-channel decoupled downsampling technique separates spatial reduction and channel increase operations, which lowers computational costs and reduces the parameter count. Furthermore, the rank-guided block design minimises redundancy within the model by adapting the complexity of different stages based on their intrinsic rank values, ensuring optimal capacity-efficiency trade-offs. YOLOv10 also introduces large-kernel (see figure 2.12) convolutions selectively in the deeper stages of the network to increase the receptive field, allowing the model to capture more contextual information without a significant increase in computational cost. Moreover, YOLOv10 incorporates a partial self-attention (PSA) mechanism, which integrates the benefits of global context modeling while maintaining a lightweight architecture.

This careful balance of efficiency and accuracy enables YOLOv10 to deliver state-of-the-art performance [45, 19].

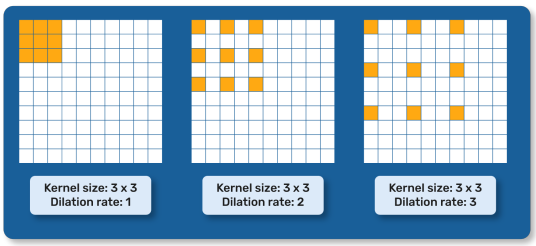

Figure 2.12: Large-Kernel Convolution in YOLOv10 [19]

As shown in table 2.1, extensive testing on standard benchmarks, such as COCO, demonstrates YOLOv10's superior performance in both speed and accuracy. For example, YOLOv10-S is 1.8 times faster than RT-DETR-R18 while also using fewer parameters. Similarly, YOLOv10-B achieves a 46% reduction in latency compared to YOLOv9-C without compromising performance. These results underscore YOLOv10's effectiveness as a real-time end-to-end object detection model, making it well-suited for applications requiring both high speed and accuracy.

Table 2.1: Performance Comparison of YOLO Models with State-of-the-Art Techniques. Latency is reported using official pre-trained models. [f]Latency refers to the forward pass duration without including post-processing. † indicates YOLOv10 results obtained with the original one-to-many training and Non-Maximum Suppression (NMS) [45].

Model	**Params (M)**	**FLOPs (G)**	**AP_{val} (%)**	**Latency[c] (ms)**	**Latency[f] (ms)**
YOLOv6-3.0-N	4.7	11.4	37.0	2.69	1.76
Gold-YOLO-N	5.6	12.1	39.6	2.92	1.82
YOLOv8-N	3.2	8.7	37.3	6.16	1.77
YOLOv10-N	**2.3**	**6.7**	**38.5 / 39.5†**	**1.84**	**1.79**
YOLOv6-3.0-S	18.5	45.3	44.3	3.42	2.35
Gold-YOLO-S	21.5	46.0	45.4	3.82	2.73
YOLO-MS-XS	4.5	17.4	43.4	8.23	2.80
YOLO-MS-S	8.1	31.2	46.2	10.12	4.83
YOLOv8-S	11.2	28.6	44.9	7.07	2.33
YOLOv9-S	7.1	26.4	46.7	-	-
RT-DETR-R18	20.0	60.0	46.5	4.58	4.49
YOLOv10-S	**7.2**	**21.6**	**46.3 / 46.8†**	**2.49**	**2.39**
YOLOv6-3.0-M	34.9	85.8	49.1	5.63	4.56
Gold-YOLO-M	41.3	87.5	49.8	6.38	5.45
YOLO-MS	22.2	80.2	51.0	12.41	7.30
YOLOv8-M	25.9	78.9	50.6	9.50	5.09
YOLOv9-M	20.0	76.3	51.1	-	-
RT-DETR-R34	31.0	92.0	48.9	6.32	6.21
RT-DETR-R50m	36.0	100.0	51.3	6.90	6.84
YOLOv10-M	**15.4**	**59.1**	**51.1 / 51.3†**	**4.74**	**4.63**

Evaluating Object Detection models involves several key metrics to measure their performance. One common metric is Intersection over Union (IoU), which measures the overlap between a predicted bounding box and a ground-truth bounding box, as shown in Figure 2.13.

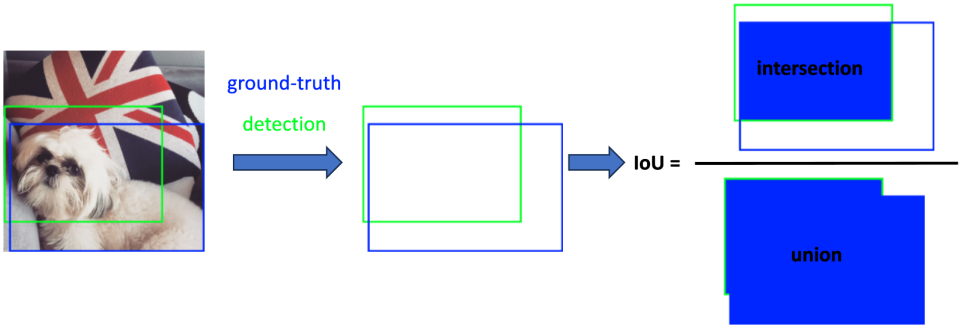

Figure 2.13: Intersection over Union (IoU) between a detection (in green) and ground-truth (in blue). [15]

Based on the IoU metric, a detection can be classified as a **True Positive (TP)** or a **False Positive (FP)** depending on whether the IoU value exceeds a certain threshold (T_{IoU}). If the IoU is above the threshold, the detection is considered correct (TP); otherwise, it is classified as a False Positive (FP). Additionally, **False Negatives (FN)** refer to ground truth objects not detected by the model, while **True Negatives (TN)** are correctly classified background detections [15]. These classifications allow for the calculation of the following metrics:

- **Precision**: The ratio of True Positives to the total number of detections, measuring the model's ability to avoid false positives:

$$\text{Precision} = \frac{\text{TP}}{\text{TP} + \text{FP}} \tag{2.1}$$

- **Recall**: The ratio of True Positives to the total number of ground-truth objects, measuring the model's ability to avoid false negatives:

$$\text{Recall} = \frac{\text{TP}}{\text{TP} + \text{FN}} \tag{2.2}$$

Common metrics used to evaluate Object Detection include:

- **Average Precision (AP)**: This combines precision and recall, providing a single figure summarizing the model's performance across different confidence thresholds. Common versions are AP@.5 (with a threshold of 0.5 IoU) and AP@[.5:.05:.95], which calculates the average of AP values over several IoU thresholds [15].
- **Average Recall (AR)**: This measures the recall of the model averaged across multiple IoU thresholds. It can be computed for different numbers of detections per image, such as AR@1, AR@10, etc. [15].
- **Inference Time**: The time taken by the model to process an image, which is critical for applications requiring real-time detection [15].
- **Model Size**: The number of parameters or the size of the model, affecting deployment, especially on devices with limited resources [15].

- **Efficiency**: This considers the trade-off between accuracy and speed, often visualized using the AP vs. inference time curve [15].

In addition to Object Detection, Object Tracking is another critical task in Computer Vision, involving the continuous monitoring of objects across video frames. Object Tracking methods can be broadly classified into two categories: **Generative Trackers** and **Discriminative Trackers** [10]. Generative trackers are capable of handling challenging scenarios such as occlusion and large-scale variation through particle sampling strategies, often integrated with various appearance models, including sparse representation and energy of motion. Discriminative trackers, by contrast, build robust classifiers using hand-crafted or deep features [10]. The combination of generative and discriminative approaches, as well as the integration of deep learning techniques such as fully revolutionary networks and Transformer models, has led to significant improvements in object detection performance [35, 56, 55]. In addition, the speed and computational requirements of these algorithms are critical factors influencing their practical applicability [56, 55, 30]. Advanced techniques in object tracking leverage both generative and discriminative models to amplify tracking efficacy. The utilisation of deep trackers has evidenced superior results on public tracking datasets, attributed to their potent feature extractors, accurate bounding box regressors, and discriminative classifiers [30]. Techniques such as deformable convolution and Transformer models extend traditional convolution or correlation methodologies to execute global feature matching, thereby enhancing tracking accuracy. The incorporation of contextual or knowledge information can substantially elevate performance, with methodologies like Particle Filtering, also recognised as Sequential Monte Carlo (SMC) methods, framed as problems of Bayesian inference in state space [12, 49]. The extended Kalman Filtering (EKF) is another advanced technique that has been employed to improve tracking accuracy by predicting the current status through the previous status and modifying the prediction result based on observation information [56, 55]. Despite these advancements, the integration of these methods in a complementary manner remains an open research area with substantial potential for advancing the field [35, 56].

2.3 Deep Learning for Spacio-Temporal Prediction

Time series prediction involves processing sequential data to predict future events or values. Various deep learning models have been applied to this task, requiring several preparatory steps such as collecting data, designating attribute types, dealing with inconsistencies and storing datasets. These datasets are usually classified into units of time such as seconds, minutes and hours, allowing the construction of metadata for machine learning [31].

Deep Learning Sequence Models

The problem of predicting the future locations of objects has been extensively studied, particularly for static surveillance cameras. Initial efforts utilised recurrent neural networks (RNNs), including long-term memory networks (LSTMs) and gated recurrent units (GRUs), in an encoder-decoder format to encode past observations and decode future locations.

Recurrent Neural Networks (RNNs), particularly Long Short-Term Memory networks (LSTMs) and Gated Recurrent Units (GRUs), have exhibited promise in this direction. Nevertheless, most RNN-based models suffer from performance degradation over time since they rely on recurrently predicting future bounding boxes based on previous outputs.

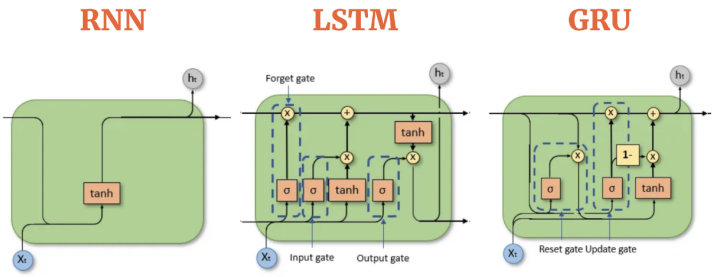

Figure 2.14: Comparing different Sequence models: RNN, LSTM, and GRU. Source: Colah's blog. Compiled by AIML.com

Early models integrated additional inputs such as environmental data and semantic actions to enhance prediction accuracy. For instance, Alahi et al. [1] proposed a Social-LSTM to model pedestrian trajectories and interactions, further improving global context capture through a social pooling module.

Deep Learning for Spatio-Temporal Prediction

STED Model

The STED (Spatio-Temporal Encoder-Decoder) model was introduced by Styles et al. [44] as a novel approach for multiple object forecasting (MOF), particularly in predicting the future bounding boxes of tracked objects from video sequences. This model is designed to handle the challenges of object forecasting in diverse environments, leveraging both visual and temporal features to predict object-motion and ego-motion effectively. As shown in figure 2.15, the STED model consists of three main components: a bounding box feature encoder, an optical flow feature encoder, and a decoder. The *Bounding Box Feature Encoder* utilises a Gated Recurrent Unit (GRU) to extract temporal features from past object bounding boxes, which

include coordinates (x, y), dimensions (w, h), and velocity changes $(\Delta x, \Delta y, \Delta w, \Delta h)$ over a window of 30 frames, representing 1 second of observation. Simultaneously, the *Optical Flow Feature Encoder* captures motion features directly from optical flow, using a Convolutional Neural Network (CNN) to process a stack of 10 frames sampled uniformly from the past 1 second of video data. The combination of these features provides a comprehensive understanding of both the object's movement and the camera's movement (ego-motion). The *Decoder* then takes the concatenated feature vector from the encoders and predicts the future bounding box coordinates for the next 60 frames (2 seconds prediction window). The GRU-based decoder generates bounding box predictions iteratively, using the encoded feature vector and the internal hidden state to output changes in bounding box velocity and dimensions over time.

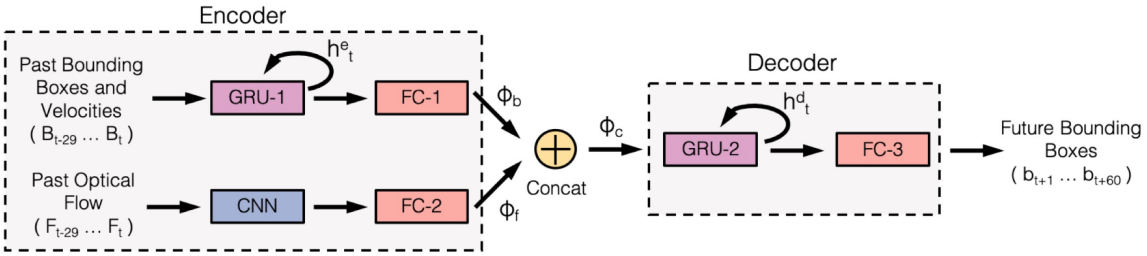

Figure 2.15: STED Model Architecture. Source: Styles et al. [44]

The STED architecture is specifically designed to address the complexities of predicting future object positions in video sequences, particularly under conditions of non-linear object motion and varying scales due to camera movement. By combining temporal features from bounding boxes with motion information from optical flow, the model effectively captures both the dynamic behavior of the objects and the impact of the camera's motion on the observed scene. The STED model was evaluated on the Citywalks dataset, a diverse dataset designed to test the model's ability to predict future object locations across different environments. The performance of STED was compared with several baseline models, as summarised in Table 2.2.

Table 2.2: Comparison of the performance of STED with baseline models on the Citywalks dataset. Metrics include Average Displacement Error (ADE), Final Displacement Error (FDE), Average Intersection-over-Union (AIoU), and Final Intersection-over-Union (FIoU). The model was evaluated using 1 second of input frames to predict 2 seconds of future frames.

Model	**ADE (pixels)**	**FDE (pixels)**	**AIoU (%)**	**FIoU (%)**
CV-CS [44]	31.6	57.6	46.0	21.3
LKF [44]	32.9	59.0	43.9	20.1
STED [44]	**26.0**	**46.9**	**51.8**	**27.5**

The STED model achieved an Average Displacement Error (ADE) of 26.0 pixels and a Final Displacement Error (FDE) of 46.9 pixels, with an Average Intersection Over Union (AIoU) of 51.8% and a Final Intersection Over Union (FIoU) of 27.5%. These results indicate that STED outperforms existing models in both displacement and intersection-over-union metrics, making it a robust solution for forecasting future object locations in challenging video sequences.

In summary, the STED model's ability to combine visual and temporal features from both object bounding boxes and optical flow enables it to predict future object positions more accurately, making it an effective tool for applications in autonomous driving and robotic navigation.

PV-LSTM Model

The PV-LSTM (Position-Velocity Long Short-Term Memory) model was developed by Bouhsain et al. [8] to predict pedestrian intentions and future bounding box positions, a crucial task for enhancing the safety of autonomous driving systems. The architecture of this model is illustrated in figure 2.16. The model utilises a sequence-to-sequence LSTM architecture that processes both spatial and temporal information effectively. To do that, it processes input sequences of observed bounding boxes (x, y, w, h) and their velocity changes $(\Delta x, \Delta y, \Delta w, \Delta h)$ over a window of 30 frames, representing 1 second of observation. These inputs are encoded through two encoders: the *Bounding Box Position Encoder* and the *Bounding Box Velocity Encoder*. The encoded features are then concatenated and passed to two decoders: the *Velocity Decoder*, which predicts future bounding box velocities, and the *Intention Decoder*, which predicts pedestrian crossing intentions over the next 60 frames (2 seconds prediction window). The PV-LSTM model's architecture is designed to capture the dynamic and complex nature of pedestrian behavior, which is crucial for real-time decision-making in autonomous driving. By integrating both position and velocity information through dual encoders, the model can more accurately predict the future movements and intentions of pedestrians, thus enhancing safety and reliability in autonomous navigation systems.

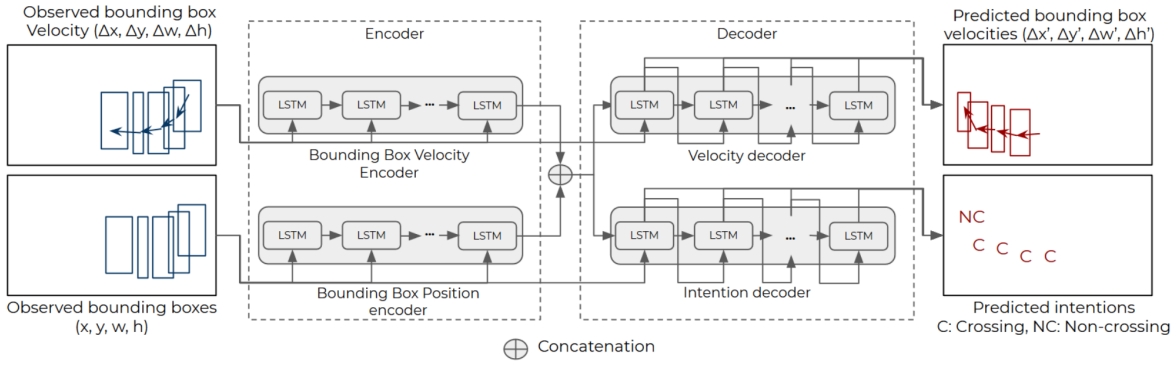

Figure 2.16: PV-LSTM Model Architecture. Source: Bouhsain et al. [8]

The PV-LSTM model was evaluated on the Citywalks dataset, and its performance was compared against several baseline models. The results are summarised in Table 2.3, showcasing the model's effectiveness in predicting pedestrian trajectories and intentions. The PV-LSTM model achieved an Average Displacement Error (ADE) of 25.2 pixels and a Final Displacement Error (FDE) of 49.9 pixels, with an Average Intersection Over Union (AIoU) of 40.2%. Although the STED model slightly outperforms in AIoU and FIoU, the PV-LSTM model provides a robust solution with competitive prediction accuracy, while maintaining a simpler architecture.

Table 2.3: Comparison of the performance of PV-LSTM with baseline models on the Citywalks dataset. Metrics include Average Displacement Error (ADE), Final Displacement Error (FDE), and Average Intersection-over-Union (AIoU). The model was evaluated using 1 second of input frames to predict 2 seconds of future frames.

Model	ADE (pixels)	FDE (pixels)	AIoU (%)	FIoU (%)
CV-CS [8]	31.6	57.6	46.0	21.3
LKF [8]	32.9	59.0	43.9	20.1
STED [8]	**26.0**	**46.9**	**51.8**	**27.5**
PV-LSTM [8]	25.2	49.9	40.2	20.3

Fusion-GRU Model

Karim et al. [28] developed the Fusion-Gated Recurrent Unit (Fusion-GRU) model to predict the future bounding boxes of traffic agents in risky driving scenarios. This model leverages multiple sources of information, such as location-scale data, monocular depth information, and optical flow data, to capture complex interactions among these cues and transform them into meaningful hidden representations. This approach is particularly suited for dealing with scenarios where the available observation time is limited due to abrupt motion changes or tracking loss. The Fusion-GRU model consists of several components that work together to predict future bounding boxes. The model takes input video sequences, extracts depth maps, and calculates optical flow to capture motion dynamics. Bounding boxes are detected and tracked using YOLOv5 and DeepSort, respectively. The feature extractor processes both object-level and scene-level features using ResNet50, transforming them into feature vectors. These vectors are then concatenated and passed to the Fusion-GRU encoder, which integrates location, scale, and distance information into hidden representations. The model also introduces an intermediary estimator, which generates intermediate bounding boxes that help in capturing sequential dependencies across frames. Additionally, a self-attention aggregation layer is employed to reduce error accumulation by focusing on the most relevant information for long-term predictions. Finally, a GRU decoder iteratively predicts the future bounding boxes based on the aggregated feature vectors and the hidden representations from the Fusion-GRU encoder.

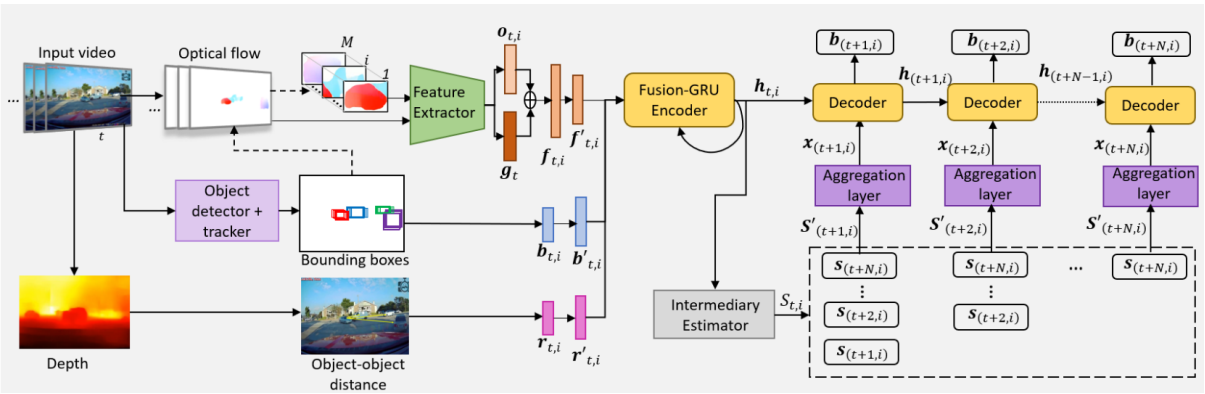

Figure 2.17: Fusion-GRU model architecture. Source: Karim et al. [28]

The Fusion-GRU model is specifically designed to address the limitations of traditional GRU-based models, which often suffer from performance degradation over time. By integrating complex interactions among various input features and employing self-attention mecha-

nisms, the Fusion-GRU model enhances its ability to predict future bounding boxes more accurately. This architecture is particularly effective in cluttered and dynamic driving environments, where understanding the relationships between different traffic agents and their surroundings is crucial for accurate prediction.

The Fusion-GRU model was evaluated on two publicly available datasets, ROL (Risky Object Localization) and HEV-I (Honda Egocentric View-Intersection), demonstrating its superior performance in predicting future bounding boxes compared to other state-of-the-art models. The results are summarised in Table 2.4, which compares the performance of Fusion-GRU with baseline models based on metrics such as Average Displacement Error (ADE), Final Displacement Error (FDE), and Intersection over Union (IOU).

Table 2.4: Comparison of the performance of Fusion-GRU with baseline models on the ROL and HEV-I datasets. Metrics include ADE, FDE, and FIoU. The model was evaluated using 0.5-second and 1-second prediction horizons.

Model	**ADE0.5 (pixels)**	**FDE0.5 (pixels)**	**FIoU0.5 (%)**	**ADE1.0 (pixels)**
FOL-X [28]	6.7	11.0	85.0	12.6
SGDNet [28]	6.3	–	–	11.4
Fusion-GRU [28]	**5.5**	**8.3**	**85.2**	**11.2**

The Fusion-GRU model achieved the lowest Average Displacement Error (ADE) and Final Displacement Error (FDE) in both 0.5-second and 1-second prediction horizons on the HEV-I dataset. It also exhibited the highest Final Intersection over Union (FIoU) of 85.2% in the 0.5-second horizon, indicating its strong capability to accurately predict the future positions and scales of traffic agents.

Chapter 3

Methodology

3.1 Dataset Configuration

3.1.1 Dataset Description

The 'Indoor Hangar Fueling Port Detection and Tracking Dataset' (HARD) is an integral part of Phase-1 of the ONEHeart project, funded by UKRI. The ONEHeart project aims to develop an automated aircraft refuelling system based on computer vision and robotics technology. This dataset can be utilised for various purposes, including but not limited to refueling port detection, fueling port tracking, camera pose estimation, and visual image processing. It is provided under the terms of the UKRI funding agreement. Unauthorised use, distribution, or reproduction is prohibited. The HARD dataset consists of 21 video sequences captured in an indoor hangar at the Aerospace Integration Research Centre (AIRC). The videos were recorded using an Intel® RealSense™ D435 [23] (Shown in Figure 3.1), which provides depth information in addition to RGB data. The target area for detection and tracking is near the refueling port of an Airbus A320 wing. The videos were recorded under different lighting conditions, including indoor artificial lighting and natural daylight, to simulate real-world scenarios. In addition, the refueling port was in different states (closed, open, and semi-open) to capture a wide range of variations for training and testing machine learning models.

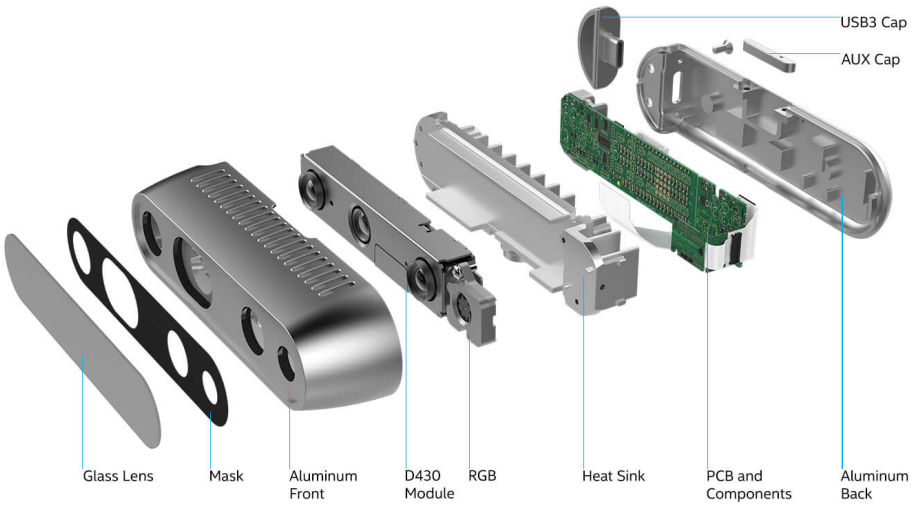

Figure 3.1: Intel® RealSense™ D435 Depth Camera. Source: Intel

3.1.2 Data Annotation

The HARD dataset provided for this project was not fully annotated. Therefore, the first step in the data preparation process was to annotate the dataset. This annotation process was crucial to enable the training of machine learning models for accurate refueling port detection and tracking. Initially, 100 frames from each video sequence were manually annotated. This involved labeling the refueling port in each frame, which required identifying and marking the exact location of the refueling port using bounding boxes. This was done using the Label Studio tool, a powerful annotation platform that allows users to create and manage annotations in images and videos. Label Studio was chosen for its flexibility and ease of use. It supports various annotation formats and integrates well with machine learning workflows. Users can draw bounding boxes around objects of interest, in this case, the refueling port, to create labeled datasets. The initial manual annotations created a preliminary dataset. This dataset was used to train a YOLOv10 (You Only Look Once, version 10) model for refueling port detection. The annotated dataset was used to train the YOLOv10 model. The model learned to detect the refueling port from the annotated images, improving its accuracy with each training iteration. After training the YOLOv10 model, it was implemented as a backend service for Label Studio. This was deployed as a Docker container, allowing the model to be used for automated annotation of the remaining images in the dataset. The model predicted the location of the refueling port in new frames, and these predictions were used to annotate the rest of the dataset automatically. Each automatically generated annotation was reviewed manually to ensure accuracy. This review process involved verifying the location of the refueling port in each frame and making necessary corrections to the annotations. This thorough quality control ensured that the entire dataset was consistently and accurately labeled.This comprehensive annotation process ensured that the entire dataset was accurately labeled, providing a robust foundation for training machine learning models aimed at refueling port detection and tracking. The combination of manual and automated annotation techniques maximised efficiency while maintaining high annotation quality.

3.1.3 Summary of Available Videos

Each video was assigned to a specific dataset (train, val, and test), with an approximate split of 70% for training, 15% for validation, and 15% for testing. The following table presents the available videos in the dataset along with the number of frames for each video and their assignment:

Type	Video Name	Number of Frames	Assignment
Closed	**video_lab_platform_1**	**624**	**train**
Closed	video_lab_platform_2	639	train
Closed	video_lab_platform_5	398	train
Closed	video_lab_platform_7	412	train
Closed	video_lab_platform_8	470	train
Closed	video_lab_platform_9	373	train
Closed	video_lab_manual_1	746	train
Closed	video_lab_platform_3	569	val
Closed	video_lab_platform_4	247	val
Closed	video_lab_platform_6	303	test
Closed	test_outdoor1	499	test
Open	**video_lab_open_1_____1**	**497**	**train**
Open	video_lab_open_1_____2	602	train
Open	video_lab_open_1_____3	313	train
Open	video_lab_open_1_____4	310	train
Open	test_indoor2	310	val
Open	test_indoor1	314	test
Semi-Open	**video_lab_semiopen_1_____1**	**739**	**train**
Semi-Open	video_lab_semiopen_1_____2	439	train
Semi-Open	video_lab_semiopen_1_____4	372	val
Semi-Open	video_lab_semiopen_1_____3	383	test

Table 3.1: Summary of available videos in the HARD dataset with their assignment.

3.1.4 Data Distribution

Before balancing the data, the distribution of video frames across the different datasets (train, validation, and test) for each state of the fueling port (CLOSED, OPEN, and SEMI-OPEN) was as follows:

Type	Total Frames	Train	Test	Validation
CLOSED	5280	3662 (69.36%)	802 (15.19%)	816 (15.45%)
OPEN	2346	1722 (73.40%)	314 (13.38%)	310 (13.21%)
SEMI-OPEN	1933	1178 (60.94%)	383 (19.81%)	372 (19.24%)

Table 3.2: Distribution of frames across train, test, and validation sets for each state in the HARD dataset before balancing.

As shown in 3.2, the dataset initially had an imbalance in the number of frames for each state. For instance, the CLOSED state had significantly more frames compared to the OPEN and SEMI-OPEN states. This imbalance could lead to biased training and inaccurate model performance, as the model might become overly familiar with the more prevalent CLOSED state and underperform on the less represented states.

3.1.5 Data Balancing

To address this issue, a balancing strategy was employed to create a more uniform dataset. The first step involved shuffling and subsetting each state (CLOSED, OPEN, and SEMI-OPEN) to keep only the minimum number of frames for each state. This ensured that the number of frames for each state was equal, avoiding bias towards any particular state. The subsets were then merged to create three balanced datasets: Training, Validation, and Test, each with an equal number of frames for each state. Finally, the balanced datasets were shuffled again and resized to maintain the required split ratio of 70% for training, 15% for validation, and 15% for testing. The balanced dataset will be used for training and evaluating the object detection model, while the full dataset will be utilised for sequence model training and framework evaluation. The resulting distribution of frames across the train, test, and validation sets for each state after balancing is as follows:

Dataset	Total Frames
Train	3534 (69.57%)
Test	773 (15.22%)
Val	773 (15.22%)

Table 3.3: Distribution of frames across train, test, and validation sets for each state in the HARD dataset after balancing.

” The primary reason for balancing the dataset is to ensure that the object detection model is equally trained on all states of the refueling port. An imbalanced dataset could cause the model to perform well on the more common states (like CLOSED) while underperforming on the less common states (like OPEN and SEMI-OPEN). By balancing the dataset, the model has an equal opportunity to learn from all states, improving its generalisation and robustness.

3.1.6 Example Images from the Datase

The following figures show annotated examples of the refueling port in different states:

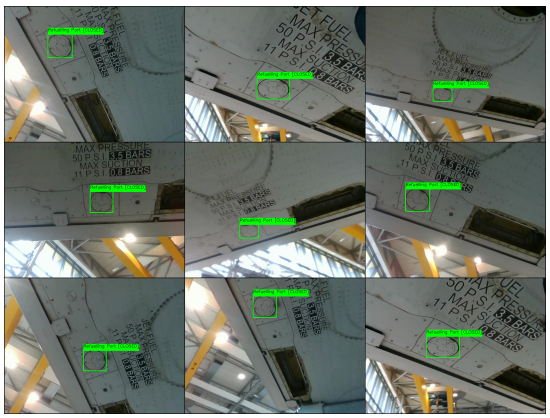

Figure 3.2: Annotated images of the refueling port in the CLOSED state.

Figure 3.3: Annotated images of the refueling port in the OPEN state.

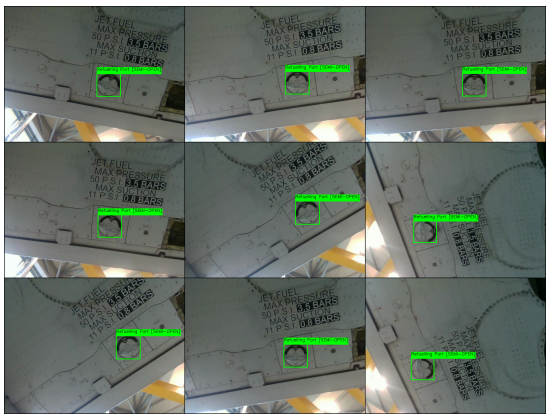

Figure 3.4: Annotated images of the refueling port in the SEMI-OPEN state.

3.1.7 Analysis of Temporal Dynamics with Savitzky-Golay Filtering

The temporal dynamics of the refueling port were analysed by examining several key metrics, including the central position, velocity, acceleration, and area over time. These metrics were extracted from video sequences and analysed in both their raw form and after applying a Savitzky-Golay filter with a small window size of 5 frames. This filtering technique is known for its ability to smooth data and reduce noise while preserving significant features, making it an ideal choice for analyzing the dynamic behavior of objects in video data. Figures 3.5 and 3.7 present the unfiltered, raw data, which captures the real-time fluctuations in the refueling port's behavior. However, due to the presence of noise, these figures can sometimes obscure the underlying patterns and trends. For example, in the raw data (Figure 3.5), the central position of the refueling port shows considerable variation, particularly in the y-axis, which may not fully represent the true motion of the port but rather include noise from sensor data or minor frame-to-frame inconsistencies. The application of the Savitzky-Golay filter, as shown in Figures 3.6 and 3.8, provides a clearer and more accurate depiction of the refueling port's movement. The central position data (Figure 3.6a) now shows a smoother trajectory, revealing the actual motion trends of the port without the distraction of short-term noise. This is particularly evident in the smoothed velocity and acceleration graphs (Figures 3.6b and 3.6c), where significant changes in motion are clearly delineated, allowing for more accurate identification of periods of acceleration or deceleration. Moreover, the analysis of the area of the bounding box (Figure 3.8d) after filtering highlights the changes in the apparent size of the refueling port with more clarity. The smoother curve suggests that the port's distance from the camera or its orientation relative to the camera lens changes gradually rather than abruptly, providing a more realistic depiction of its dynamics.

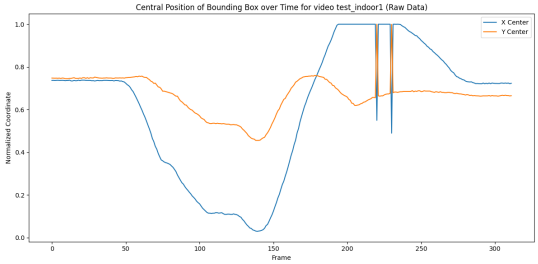

(a) Central position of the refueling port over time (Raw Data).

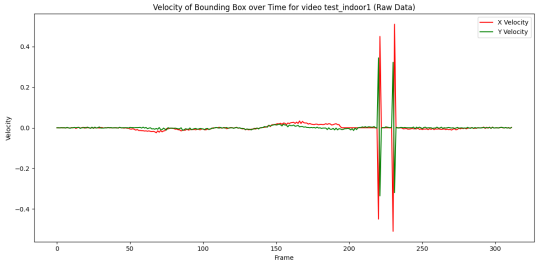

(b) Velocity of the refueling port over time (Raw Data).

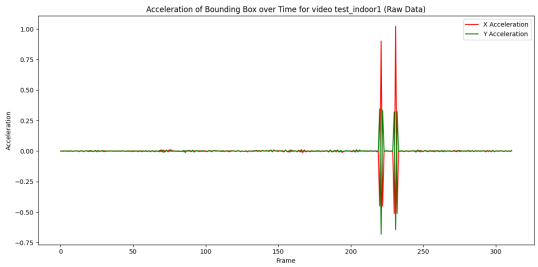

(c) Acceleration of the refueling port over time (Raw Data).

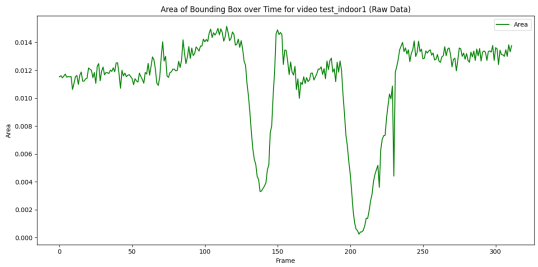

(d) Area of the refueling port over time (Raw Data).

Figure 3.5: Temporal analysis of different metrics for the refueling port in the *test_indoor1* video (Raw Data). The metrics include (a) central position, (b) velocity, (c) acceleration, and (d) area, providing an overview of the object's dynamics over time.

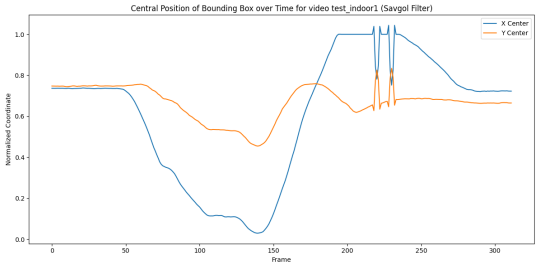

(a) Central position of the refueling port over time (Savgol Filter).

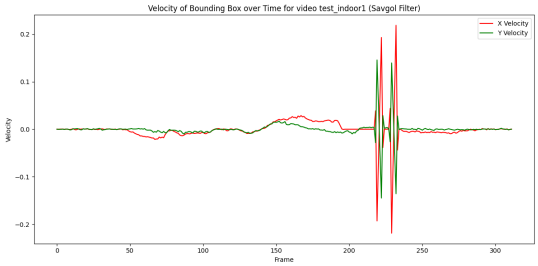

(b) Velocity of the refueling port over time (Savgol Filter).

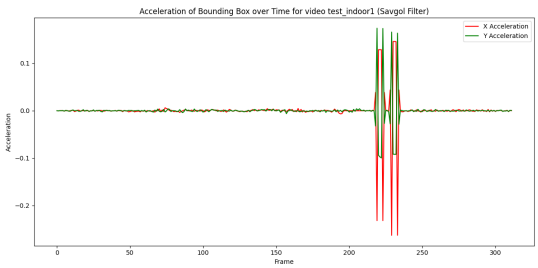

(c) Acceleration of the refueling port over time (Savgol Filter).

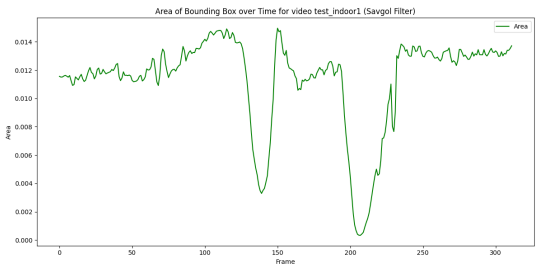

(d) Area of the refueling port over time (Savgol Filter).

Figure 3.6: Temporal analysis of different metrics for the refueling port in the *test_indoor1* video (Savgol Filter). The metrics include (a) central position, (b) velocity, (c) acceleration, and (d) area, providing a clearer overview of the object's dynamics over time after applying the Savitzky-Golay filter.

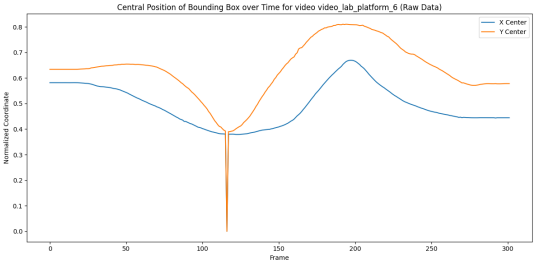

(a) Central position of the refueling port over time (Raw Data).

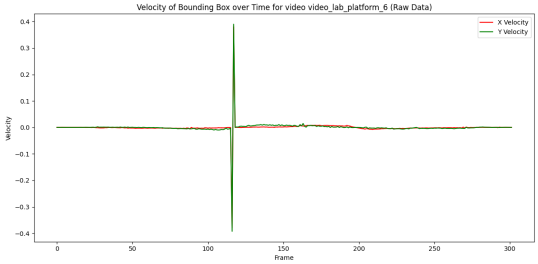

(b) Velocity of the refueling port over time (Raw Data).

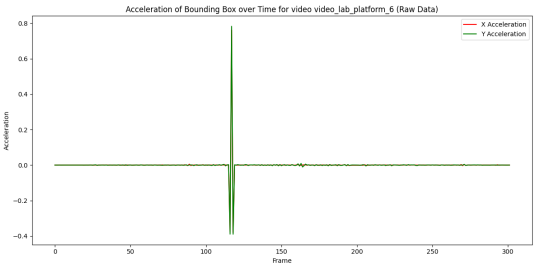

(c) Acceleration of the refueling port over time (Raw Data).

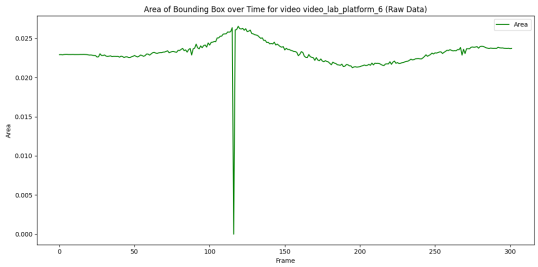

(d) Area of the refueling port over time (Raw Data).

Figure 3.7: Temporal analysis of different metrics for the refueling port in the *test_video_lab_platform_6* video (Raw Data). The metrics include (a) central position, (b) velocity, (c) acceleration, and (d) area, providing an overview of the object's dynamics over time.

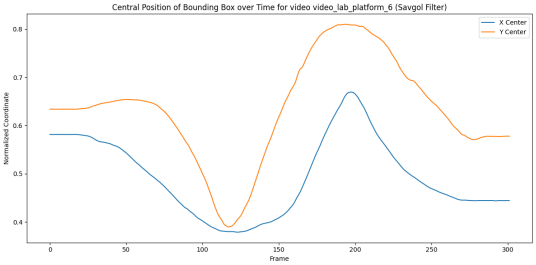

(a) Central position of the refueling port over time (Savgol Filter).

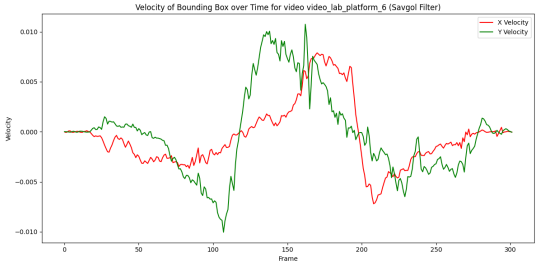

(b) Velocity of the refueling port over time (Savgol Filter).

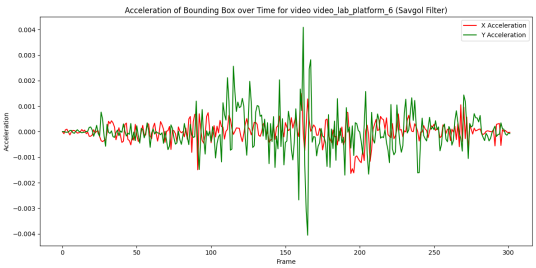

(c) Acceleration of the refueling port over time (Savgol Filter).

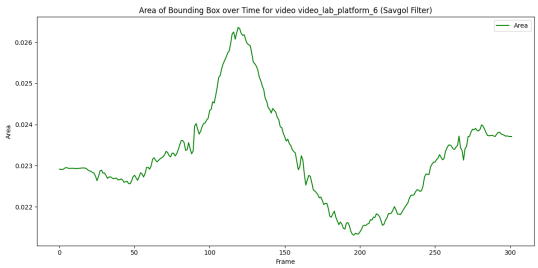

(d) Area of the refueling port over time (Savgol Filter).

Figure 3.8: Temporal analysis of different metrics for the refueling port in the *test_video_lab_platform_6* video (Savgol Filter). The metrics include (a) central position, (b) velocity, (c) acceleration, and (d) area, providing a clearer overview of the object's dynamics over time after applying the Savitzky-Golay filter.

3.2 Framework Design

The proposed framework, illustrated in Figure 3.9, is designed to predict the future positions of the refueling port's bounding boxes across the next m frames of a video stream. It does this by leveraging the bounding boxes observed in the current and previous frames. At any given time step t, the observed bounding box is denoted as $\mathbf{b}_t = [x_t, y_t, w_t, h_t]$, where (x_t, y_t) represents the center coordinates of the bounding box, and w_t and h_t represent the width and height of the bounding box, respectively. The goal is to predict a sequence of future bounding boxes, $\mathbf{S}_{t+1:t+m} = \{\mathbf{b}_{t+1}, \ldots, \mathbf{b}_{t+m}\}$, for the upcoming m frames based on the observed bounding boxes from the past n frames, $\mathbf{S}_{t-1+n:t} = \{\mathbf{b}_{t-1+n}, \ldots, \mathbf{b}_t\}$.

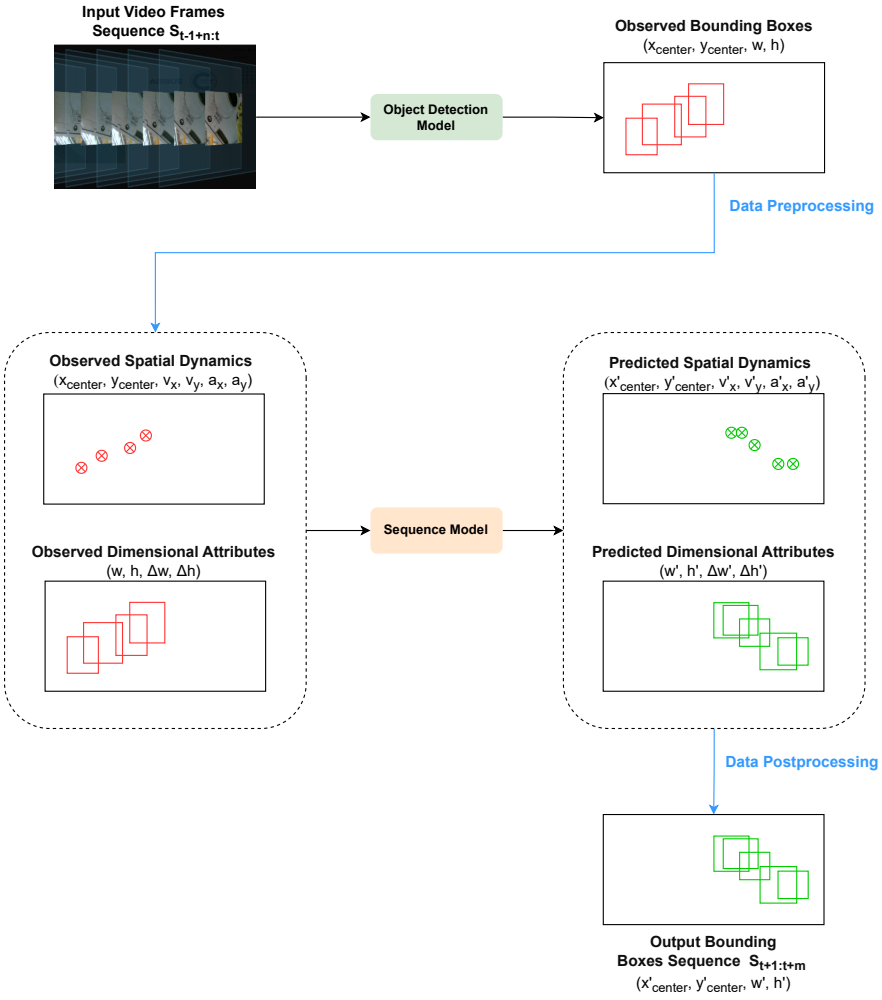

Figure 3.9: Framework Workflow

The process starts with an input video sequence, which is analysed on a frame-by-frame basis. An object detection model first identifies and locates the bounding boxes of the refueling port in each frame. These detected bounding boxes are then formatted into input vectors suitable for the sequence model. The sequence model is responsible for predicting the future spatial positions and dimensions of the refueling port's bounding boxes. Finally, these predictions are refined through postprocessing steps to produce the final bounding box forecasts for the subsequent frames.

3.3 Object Detection Model Fine-tuning

A fine-tuned YOLOv10 Nano model is used to detect the refueling port within the video frames. As highlighted in the literature review, YOLOv10 represents the latest advancement in object detection technology, offering an optimal balance between speed and accuracy. The YOLOv10 Nano variant is particularly well-suited for real-time applications, especially on resource-constrained embedded devices, due to its lightweight architecture. The model is fine-tuned through transfer learning on the HARD dataset, enabling precise detection of the refueling port within the video frames. This fine-tuning process ensures that the model meets the demands of real-time video analysis with both accuracy and responsiveness. The implementation uses the Ultralytics YOLOv10 framework [26], which provides a reliable and efficient pipeline for both training and inference. This framework optimises detection performance and guarantees robust operation in different scenarios.

3.4 Sequence Model Design

This thesis introduces the *SizPos-GRU* model, a deep learning sequence model for predicting future positions and sizes of a unique object in a video stream. The model leverages an encoder-attention-decoder architecture to capture temporal dependencies and spatial relationships effectively. The SizPos-GRU model leverages an encoder-attention-decoder architecture to effectively capture temporal dependencies and spatial relationships. The framework consists of four main components: two encoders, an attention mechanism, and two decoders. Each component is designed to handle specific aspects of the sequence modeling task, from encoding input sequences to generating context-aware predictions.

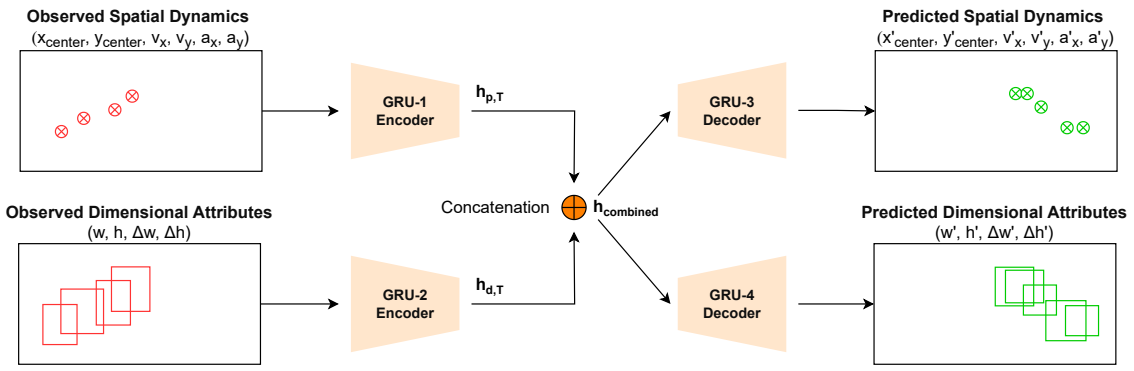

Figure 3.10: SizPos-GRU Model Architecture

3.4.1 Input Representation

The *SizPos-GRU* model expects two types of input sequences to predict the future positions and sizes of an object. The first input captures the spatial dynamics of the object, including its position, velocity and acceleration. The second input focuses on the object's dimensional attributes, such as its width and height, and changes in these dimensions over time.

Spatial Dynamics Vector

The spatial dynamics vector at time t, denoted as $\mathbf{p}_t$, represents the position, velocity, and acceleration of the bounding box center. It is defined as:

$$\mathbf{p}_t = (x_t, y_t, v_{x,t}, v_{y,t}, a_{x,t}, a_{y,t}), \tag{3.1}$$

$$v_{x,t} = x_t - x_{t-1}, \quad v_{y,t} = y_t - y_{t-1}, \tag{3.2}$$

$$a_{x,t} = v_{x,t} - v_{x,t-1}, \quad a_{y,t} = v_{y,t} - v_{y,t-1}. \tag{3.3}$$

Here, (x_t, y_t) represents the center coordinates at time t, $(v_{x,t}, v_{y,t})$ are the velocities, and $(a_{x,t}, a_{y,t})$ are the accelerations along the x and y axes, respectively.

Dimensional Attributes Vector

The dimensional attributes vector at time t, denoted as $\mathbf{d}_t$, captures the size of the bounding box and the changes in its dimensions:

$$\mathbf{d}_t = (w_t, h_t, \Delta w_t, \Delta h_t), \tag{3.4}$$

$$\Delta w_t = w_t - w_{t-1}, \quad \Delta h_t = h_t - h_{t-1}. \tag{3.5}$$

Here, (w_t, h_t) represents the width and height at time t, and $(\Delta w_t, \Delta h_t)$ are the changes in these dimensions from the previous time step.

Input Sequences for Model

The sequences of these vectors over a time window of n frames are fed into the model as:

$$\mathbf{P} = \{\mathbf{p}_{t-1+n}, \mathbf{p}_{t-n+2}, \ldots, \mathbf{p}_t\}, \quad \mathbf{D} = \{\mathbf{d}_{t-1+n}, \mathbf{d}_{t-n+2}, \ldots, \mathbf{d}_t\},$$

where $\mathbf{P}$ is the sequence of spatial dynamics vectors, and $\mathbf{D}$ is the sequence of dimensional attributes vectors. These sequences are processed by the model's encoders to extract temporal features, which are then used to predict future bounding box positions and sizes.

3.4.2 Encoders

The SizPos-GRU model employs two separate GRU encoders: one for processing the sequence of spatial dynamics vectors and another for processing the sequence of dimensional attributes vectors. Both encoders are designed to extract meaningful temporal features from their respective input sequences, which are subsequently used by the decoders to generate predictions.

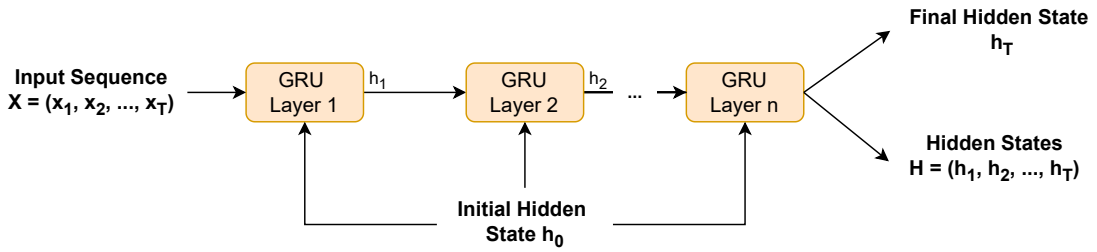

Figure 3.11: SizPos-GRU Encoder Architecture. The input sequence $\mathbf{X} = \{\mathbf{x}_1, \mathbf{x}_2, \ldots, \mathbf{x}_T\}$ represents either the spatial dynamics vector (**P**) or the dimensional attributes vector (**D**). This sequence is processed through multiple GRU layers, producing a sequence of hidden states $H = \{h_1, h_2, \ldots, h_T\}$ and a final hidden state h_T that encapsulates the temporal dependencies in the input sequence.

Position Encoder

The position encoder processes the sequence of spatial dynamics vectors, which include the bounding box's position, velocity, and acceleration over time. It is defined as:

$$H_p, h_{p_T} = \text{GRU}_p(\mathbf{P}, h_{p_0}), \tag{3.6}$$

where $\mathbf{P} = (\mathbf{p}_{t-1+n}, \mathbf{p}_{t-n+2}, \ldots, \mathbf{p}_t)$ is the input sequence of spatial dynamics vectors, $H_p = (h_{p_1}, h_{p_2}, \ldots, h_{p_T})$ represents the sequence of hidden states generated by the GRU, and h_{p_T} is the final hidden state at time T. The initial hidden state h_{p_0} is typically initialised to zero.

Size Encoder

The size encoder processes the sequence of dimensional attributes vectors, which include the bounding box's width, height, and changes in these dimensions over time. It is defined as:

$$H_d, h_{d_T} = \text{GRU}_d(\mathbf{D}, h_{d_0}), \tag{3.7}$$

where $\mathbf{D} = (\mathbf{d}_{t-1+n}, \mathbf{d}_{t-n+2}, \ldots, \mathbf{d}_t)$ is the input sequence of dimensional attributes vectors, $H_d = (h_{d_1}, h_{d_2}, \ldots, h_{d_T})$ represents the sequence of hidden states generated by the GRU, and h_{d_T} is the final hidden state at time T. Similarly, the initial hidden state h_{d_0} is initialised to zero.

3.4.3 Hidden State Fusion

After the position and size encoders process their respective input sequences, the resulting hidden states are combined to leverage information from both spatial dynamics and dimensional attributes. This fusion is achieved by concatenating the final hidden states from both encoders and passing them through a fully connected layer:

$$h_{\text{combined}} = W_{\text{combine}} \cdot [h_{p_T} \oplus h_{d_T}] + b_{\text{combine}}, \tag{3.8}$$

where h_{p_T} and h_{d_T} are the final hidden states from the position and size encoders, respectively, $\oplus$ denotes the concatenation operation, W_{combine} is the weight matrix, and b_{combine} is the bias vector. The fused hidden state h_{combined} encapsulates the temporal features from both input sequences, enabling the model to generate context-aware predictions.

3.4.4 Decoders

The *SizPos-GRU* model utilises two specialised decoders to predict the future bounding boxes over the next m frames. These decoders are designed to process the temporal features extracted by the encoders and the fused hidden states, generating accurate and context-aware predictions.

Position Decoder

The position decoder is responsible for predicting the future spatial dynamics of the bounding boxes, including their positions and velocities. The decoding process begins by initialising the input with the last observed position in the sequence. The decoder then iteratively predicts future positions over the defined prediction horizon m. During each iteration, the current input is processed through a stack of GRU layers, which update the hidden state based on the previous hidden state and current input. This updated hidden state, encapsulating temporal dependencies, is then passed through a self-attention mechanism. The self-attention mechanism computes attention scores, which are normalised using a softmax function to produce attention weights. These weights are applied to the hidden states to generate a context vector that highlights the most relevant temporal features.

$$H_p = \text{GRU}p(h\text{combined}), \tag{3.9}$$

$$\alpha_i = \frac{\exp(w_i)}{\sum_{j=1}^{m} \exp(w_j)}, \quad w_i = \text{Linear}(h_{p_i}), \tag{3.10}$$

$$c_p = \sum_{i=1}^{m} \alpha_i h_{p_i}, \tag{3.11}$$

The context vector c_p is then passed through a series of fully connected layers, with dropout and ReLU activation functions, to produce the final position prediction for the current time step:

$$\hat{\mathbf{P}}_{t+1:m} = \text{ReLU}(\text{Dropout}(\text{Dense1}(c_p))), \tag{3.12}$$

$$\hat{\mathbf{P}}t+1:m = \text{Dense2}(\hat{\mathbf{P}}t+1:m), \tag{3.13}$$

The predicted position is then used as the input for the next iteration of the decoding loop, enabling the model to recursively generate predictions for subsequent time steps. This iterative process continues until predictions for all future time steps within the prediction window have been generated, and the accumulated sequence of predicted positions is returned as the final output.

Size Decoder

The size decoder operates similarly to the position decoder but focuses on predicting the future dimensions of the bounding boxes, such as width and height. The decoding process starts with the last observed size in the sequence, and the decoder iteratively generates predictions for future sizes over the prediction horizon m. In each iteration, the current size input is processed through GRU layers that capture the temporal dynamics of size changes. The output from the GRU is then passed through a self-attention mechanism, which assigns different weights to the hidden states across time. These weights are used to compute a context vector c_d, which represents the most relevant temporal and spatial information for the current prediction step.

$$H_d = \text{GRU}d(h\text{combined}), \tag{3.14}$$

$$\beta_i = \frac{\exp(v_i)}{\sum_{j=1}^{m} \exp(v_j)}, \quad v_i = \text{Linear}(h_{d_i}), \tag{3.15}$$

$$c_d = \sum_{i=1}^{m} \beta_i h_{d_i}, \tag{3.16}$$

The context vector c_d is passed through dense layers with dropout and ReLU activation to produce the final size prediction:

$$\hat{\mathbf{D}}_{t+1:m} = \text{ReLU}(\text{Dropout}(\text{Dense1}(c_d))), \tag{3.17}$$

$$\hat{\mathbf{D}}t + 1 : m = \text{Dense2}(\hat{\mathbf{D}}t + 1 : m), \tag{3.18}$$

Similar to the position decoder, the predicted size is then used as input for the next iteration, ensuring that each prediction is contextually informed by previous outputs. This loop continues until the decoder has generated predictions for all future time steps within the prediction window m, which are then returned as the sequence of predicted sizes.

Self-Attention Mechanism

The self-attention mechanism plays a pivotal role in both decoders by enhancing the model's ability to focus on the most relevant parts of the input sequences. By dynamically assigning weights to different time steps, the self-attention mechanism allows the model to capture long-range dependencies, which are crucial for accurate predictions over extended time horizons.

Final Output

The final output of the decoding process consists of sequences of predicted positions and sizes for the specified number of future time steps m. These predictions provide valuable insights into the expected future states of the bounding boxes, including their movement and changes in dimensions. The integration of GRU layers and self-attention mechanisms within the decoders ensures that the *SizPos-GRU* model can effectively handle complex sequence prediction tasks, making it well-suited for applications such as video analysis and object tracking.

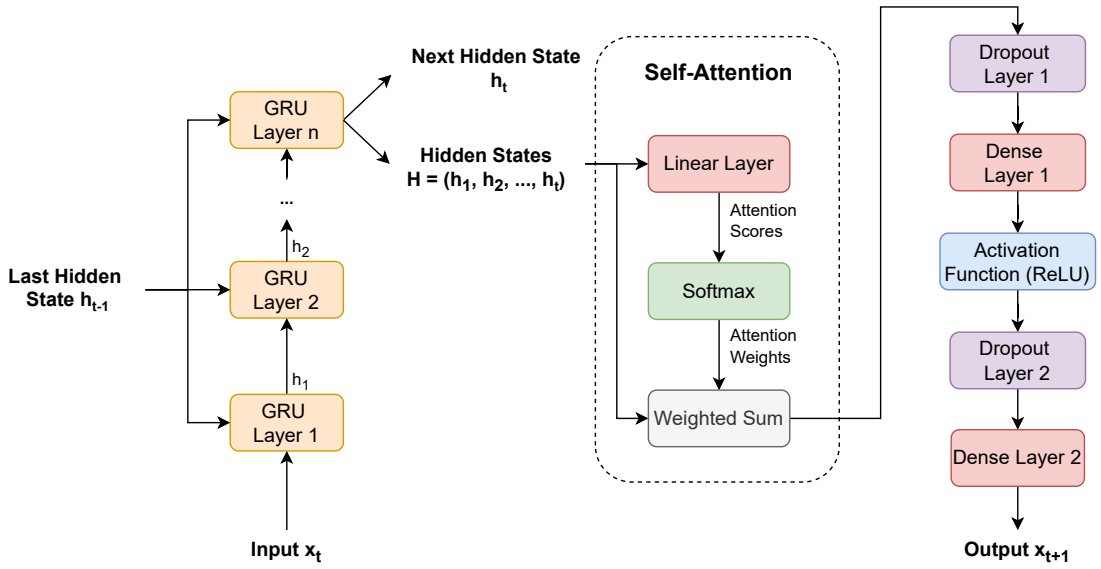

Figure 3.12: SizPos-GRU Decoder Architecture. This architecture illustrates the decoding process where the input sequence $\mathbf{x}_t$ and the last hidden state h_{t-1} are processed through multiple GRU layers to generate the next hidden state h_t. The sequence of hidden states $H = \{h_1, h_2, \ldots, h_t\}$ is then passed through a self-attention mechanism, which calculates attention scores and weights. The weighted sum of hidden states is combined with linear and non-linear transformations, including dropout and ReLU activation functions, to produce the final output $\mathbf{x}_{t+1}$. This output is used for predicting the next time step in the sequence, continuing the process iteratively for future predictions.

3.5 Algorithm Design

3.5.1 Calculation of Key Values for Loss Functions

In the SizPos-GRU model, several values are calculated to derive the loss functions that guide the model training and optimisation process. These values are obtained by transforming the model's raw outputs into meaningful metrics that can be compared with the ground truth data. The key values calculated include:

Bounding Box and Velocity Estimation

For each time step t, the model predicts spatial dynamics $\hat{\mathbf{p}}_t$ and dimensional attributes $\hat{\mathbf{d}}_t$. These predictions are used to estimate bounding boxes and velocities:

$$\hat{b}_{x,t} = \hat{p}_{x,t}, \tag{3.19}$$
$$\hat{b}_{y,t} = \hat{p}_{y,t}, \tag{3.20}$$
$$\hat{b}_{w,t} = \hat{d}_{w,t}, \tag{3.21}$$
$$\hat{b}_{h,t} = \hat{d}_{h,t}, \tag{3.22}$$
$$\hat{v}_{x,t} = \hat{p}_{x,t} - \hat{p}_{x,t-1}, \tag{3.23}$$
$$\hat{v}_{y,t} = \hat{p}_{y,t} - \hat{p}_{y,t-1}, \tag{3.24}$$
$$\hat{v}_{w,t} = \hat{d}_{w,t} - \hat{d}_{w,t-1}, \tag{3.25}$$
$$\hat{v}_{h,t} = \hat{d}_{h,t} - \hat{d}_{h,t-1}. \tag{3.26}$$

Where $\hat{b}_{x,t}, \hat{b}_{y,t}, \hat{b}_{w,t}, \hat{b}_{h,t}$ represent the predicted bounding box's center coordinates, width, and height at time t, and $\hat{v}_{x,t}, \hat{v}_{y,t}, \hat{v}_{w,t}, \hat{v}_{h,t}$ represent the corresponding velocities.

Velocity to Position Conversion

To derive future positions from the predicted velocities, the following equations are used:

$$\hat{p}_{x,t+1} = \hat{p}_{x,t} + \hat{v}_{x,t}, \tag{3.27}$$
$$\hat{p}_{y,t+1} = \hat{p}_{y,t} + \hat{v}_{y,t}, \tag{3.28}$$
$$\hat{d}_{w,t+1} = \hat{d}_{w,t} + \hat{v}_{w,t}, \tag{3.29}$$
$$\hat{d}_{h,t+1} = \hat{d}_{h,t} + \hat{v}_{h,t}. \tag{3.30}$$

These equations are used iteratively to predict the positions and sizes at each future time step, integrating the model's output over time.

3.5.2 Loss Function Formulation

To train the SizPos-GRU model, Smooth L1 Loss, also known as Huber Loss, a composite loss function is employed, which takes into account various aspects of prediction accuracy. This loss function is a combination of L1 and L2 losses, providing a balance between the two, making it less sensitive to outliers than L2 loss while avoiding the large gradient changes associated with L1 loss. The loss functions have been applied to various aspects of the model predictions:

Size and Position Loss

The model calculates the Smooth L1 Loss for the predicted sizes and positions compared to the ground truth data:

$$\mathscr{L}_{\text{size}} = \frac{1}{N}\sum_{t=1}^{m}\sum_{i\in\{w,h\}} \text{SmoothL1}\left(\hat{d}_{i,t}, d_{i,t}^{gt}\right), \tag{3.31}$$

$$\mathscr{L}_{\text{position}} = \frac{1}{N}\sum_{t=1}^{m}\sum_{i\in\{x,y\}} \text{SmoothL1}\left(\hat{p}_{i,t}, p_{i,t}^{gt}\right). \tag{3.32}$$

Where $\text{SmoothL1}(a,b)$ is defined as:

$$\text{SmoothL1}(a,b) = \begin{cases} 0.5\times(a-b)^2 & \text{if } |a-b|<1 \\ |a-b|-0.5 & \text{otherwise.} \end{cases} \tag{3.33}$$

Bounding Box Loss

The model also computes the loss for the predicted bounding boxes, which represent the object's position and size in a unified format. The bounding box at each time step t is given by $\hat{\mathbf{b}}_t = (\hat{b}_{x,t}, \hat{b}_{y,t}, \hat{b}_{w,t}, \hat{b}_{h,t})$. The loss for these predictions is calculated as:

$$\mathscr{L}_{\text{bbox}} = \frac{1}{N}\sum_{t=1}^{m}\sum_{i\in\{x,y,w,h\}} \text{SmoothL1}\left(\hat{b}_{i,t}, b_{i,t}^{gt}\right), \tag{3.34}$$

where $b_{i,t}^{gt}$ represents the ground truth bounding box coordinates and dimensions at time t.

Velocity-to-Position Loss

To ensure that the predicted velocities accurately translate to future positions, the model includes a loss term that compares the predicted positions derived from velocities ($\hat{p}_{x,t+1}$, $\hat{p}_{y,t+1}$, $\hat{d}_{w,t+1}$, $\hat{d}_{h,t+1}$) with the ground truth positions and sizes at the next time step:

$$\mathscr{L}_{\text{vel-to-pos}} = \frac{1}{N}\sum_{t=1}^{m}\sum_{i\in\{x,y,w,h\}} \text{SmoothL1}\left(\hat{p}_{i,t+1}, p_{i,t+1}^{gt}\right). \tag{3.35}$$

This loss term ensures that the model's predicted velocities are consistent with the subsequent positions, reinforcing the temporal coherence of the predictions.

Total Loss

The total loss used for model training is the sum of all the individual losses:

$$\mathscr{L}_{\text{total}} = \mathscr{L}_{\text{size}} + \mathscr{L}_{\text{position}} + \mathscr{L}_{\text{bbox}} + \mathscr{L}_{\text{vel-to-pos}}. \tag{3.36}$$

3.5.3 Data Postprocessing

Post-processing is a crucial step in the proposed prediction pipeline that refines the raw predictions generated by the model. The main objective is to enhance the accuracy and smoothness of the predicted bounding box trajectories of the aircraft refueling port. Several smoothing techniques are applied to reduce noise and eliminate unrealistic variations in the predicted trajectories. These techniques ensure that the final output is both accurate and visually coherent.

Savitzky-Golay Filter

The Savitzky-Golay filter is a digital filter used to smooth data while preserving its shape and features. It works by fitting successive subsets of data points with a low-degree polynomial. The filter is particularly effective in reducing noise without significantly distorting the signal. Given a trajectory $\mathbf{y} = \{y_1, y_2, \ldots, y_n\}$, the smoothed value at point i is obtained by fitting a polynomial of degree k over a window of size $2m+1$ centered at i:

$$\hat{y}_i = \sum_{j=-m}^{m} c_j y_{i+j}, \tag{3.37}$$

where c_j are the coefficients determined by the polynomial fit.

Moving Average Smoothing

Moving average smoothing is a simple technique that calculates the average of a sliding window of data points, effectively reducing short-term fluctuations and highlighting longer-term trends. For a given trajectory $\mathbf{y}$, the smoothed value at point i using a window of size w is computed as:

$$\hat{y}_i = \frac{1}{w} \sum_{j=0}^{w-1} y_{i-j}. \tag{3.38}$$

This method is straightforward and helps to smooth out irregularities in the trajectory.

Exponential Smoothing

Exponential smoothing assigns exponentially decreasing weights to past observations, making it suitable for time-series data where recent data points are more relevant. The smoothed value at time t is given by:

$$\hat{y}_t = \alpha y_t + (1-\alpha)\hat{y}_{t-1}, \tag{3.39}$$

where α is the smoothing factor, $0 < \alpha \leq 1$, and $\hat{y}_{t-1}$ is the previously smoothed value.

Adaptive Smoothing

Adaptive smoothing adjusts the degree of smoothing based on the variation observed in the data. If a significant change is detected between consecutive data points, more aggressive smoothing is applied. Given a trajectory $\mathbf{y}$, the adaptive smoothing is defined as:

$$\hat{y}_t = \begin{cases} \text{Smooth}(\mathbf{y}_{t-k:t}) & \text{if } |y_t - y_{t-1}| > \text{threshold}, \\ y_t & \text{otherwise}, \end{cases} \tag{3.40}$$

where $\text{Smooth}(\mathbf{y}_{t-k:t})$ applies a smoothing filter over the recent k data points.

Hybrid Smoothing

Hybrid smoothing combines multiple smoothing techniques to leverage their strengths. Typically, a Savitzky-Golay filter is applied first, followed by a moving average smoothing on the already smoothed trajectory. Let $\hat{\mathbf{y}}^{(1)}$ be the output of the Savitzky-Golay filter applied to $\mathbf{y}$. The final smoothed trajectory $\hat{\mathbf{y}}^{(2)}$ is obtained by applying a moving average:

$$\hat{\mathbf{y}}^{(2)} = \frac{1}{w} \sum_{j=0}^{w-1} \hat{y}_{i-j}^{(1)}, \tag{3.41}$$

where w is the window size for the moving average.

Kalman Filter Smoothing

The Kalman Filter is a statistical method used to estimate the state of a dynamic system from a series of noisy measurements. In our context, it is used to smooth the predicted bounding box trajectories by estimating the underlying motion parameters. The Kalman Filter operates in two main steps: prediction and update.The predicted state $\mathbf{x}_{t|t-1}$ and its covariance $\mathbf{P}_{t|t-1}$ are computed as:

$$\mathbf{x}_{t|t-1} = \mathbf{F}\mathbf{x}_{t-1|t-1}, \tag{3.42}$$

$$\mathbf{P}_{t|t-1} = \mathbf{F}\mathbf{P}_{t-1|t-1}\mathbf{F}^T + \mathbf{Q}, \tag{3.43}$$

where $\mathbf{F}$ is the state transition matrix, and $\mathbf{Q}$ is the process noise covariance matrix. The update step corrects the prediction using the actual measurement $\mathbf{z}_t$:

$$\mathbf{K}_t = \mathbf{P}_{t|t-1}\mathbf{H}^T(\mathbf{H}\mathbf{P}_{t|t-1}\mathbf{H}^T + \mathbf{R})^{-1}, \tag{3.44}$$

$$\mathbf{x}_{t|t} = \mathbf{x}_{t|t-1} + \mathbf{K}_t(\mathbf{z}_t - \mathbf{H}\mathbf{x}_{t|t-1}), \tag{3.45}$$

$$\mathbf{P}_{t|t} = (\mathbf{I} - \mathbf{K}_t\mathbf{H})\mathbf{P}_{t|t-1}, \tag{3.46}$$

where $\mathbf{K}_t$ is the Kalman gain, $\mathbf{H}$ is the measurement matrix, and $\mathbf{R}$ is the measurement noise covariance.

Chapter 4

Experiment Design

4.1 Experiment Environment

The experiments were conducted using a high-performance computing environment optimised for deep learning tasks. The hardware configuration included an NVIDIA A40 GPU with 48 GB of VRAM, 9 virtual CPUs (vCPUs), and 50 GB of RAM, ensuring efficient handling of large-scale models and data processing tasks. The software environment was based on a Linux operating system, utilising PyTorch Lightning [16] for sequence model implementation. PyTorch Lightning provided a streamlined and modular framework, improving experimentation and reproducibility. Data loading was managed using PyTorch's `DataLoader` [2] with 8 worker threads to maximise I/O efficiency.

4.2 Model Training and Optimization

Model Parameters

The SizPos-GRU model was trained using the Adam optimizer, which is known for its ability to adapt learning rates for each parameter, enhancing the convergence speed and stability of the training process. Adam computes adaptive learning rates for each parameter by keeping track of both the first and second moments of the gradients. This optimizer was selected due to its proven efficiency in handling non-stationary objectives and noisy gradients, which are common in deep learning models. The learning rate was dynamically adjusted using a *ReduceLROnPlateau* scheduler. This scheduler is particularly effective in preventing the model from getting stuck in local minima by reducing the learning rate when the validation loss stops improving. The learning rate $\mathrm{LR}_{\mathrm{new}}$ is updated according to the following rule:

$$\mathrm{LR}_{\mathrm{new}} = \mathrm{LR}_{\mathrm{current}} \times \mathrm{scheduler\_factor}, \tag{4.1}$$

where scheduler_factor is a predefined factor, typically set to a value less than 1, which controls how significantly the learning rate is reduced. This approach allows the model to make finer updates as it converges, thereby improving the chances of finding a better local minimum. The training was conducted with close monitoring of validation performance to ensure the model's ability to generalise to unseen data. By using early stopping based on validation metrics, the training process was made more efficient, preventing overfitting and ensuring that the model retained its ability to perform well on new data. Table 4.1 provides an overview of the training

configuration parameters used for the SizPos-GRU model. These parameters were selected based on the optimal results obtained from extensive hyperparameter tuning.

Table 4.1: Training Configuration Parameters for the SizPos-GRU Model. The values were selected based on optimal results from hyperparameter tuning.

Parameter	Description	Value
Random Seed	Seed value for reproducibility	42
Number of Workers	Number of CPU cores used for data loading	8
Batch Size	Number of samples per batch during training	64
Input Frames	Number of input frames fed into the model	15, 30
Output Frames	Number of frames predicted by the model	30, 60
Hidden Layer Size	Size of the hidden layers in the GRU network	128, 256
Number of Layers	Number of GRU layers stacked in the network	8
Learning Rate	Initial learning rate for the optimizer	5×10^{-4}
Scheduler Patience	Number of epochs to wait before reducing the learning rate	10 epochs
Scheduler Factor	Factor by which the learning rate is reduced	0.9
Max Epochs	Maximum number of epochs for training	100
Dropout Rate	Probability of dropping a neuron during training	0.2
Optimizer	Optimization algorithm used for training	Adam
Scheduler	Learning rate scheduler used for dynamic adjustment	ReduceLROnPlateau
Checkpoint Metric	Metric used to save the best model checkpoint	Best Final Intersection over Union (FIOU)

Hyperparameter Tuning

Extensive hyperparameter tuning was conducted to determine the most effective configurations for the SizPos-GRU model. This process involved systematically varying key parameters to assess their impact on model performance. The goal was to strike a balance between model complexity and computational efficiency while ensuring that the model could learn effectively from the available data. Table 4.2 summarises the hyperparameter tuning configuration, listing the range of values tested for each parameter. The tuning process included exploring different sizes and numbers of hidden layers, varying the number of input and output frames, and adjusting the learning rate, among other factors.

Table 4.2: Hyperparameter Tuning Configuration

Parameter	Description	Values Tested
Input Frames	Number of input frames fed into the model	15, 30
Output Frames	Number of frames predicted by the model	30, 60
Hidden Layer Sizes	Size of the hidden layers in the GRU network	32, 64, 128, 256, 512
Number of Hidden Layers	Number of GRU layers stacked in the network	1, 2, 4, 8
Learning Rate	Initial learning rate for the optimizer	5×10^{-4}
Scheduler Patience	Number of epochs to wait before reducing the learning rate	10 epochs
Scheduler Factor	Factor by which the learning rate is reduced	0.9
Max Epochs	Maximum number of epochs for training	100
Dropout Rate	Probability of dropping a neuron during training	0.2

The final selection of hyperparameters, informed by the tuning results, was critical in ensuring the SizPos-GRU model's effectiveness. The chosen parameters provided a balance that allowed the model to perform well across different scenarios while maintaining computational efficiency. This careful calibration was essential for achieving the desired model accuracy and robustness during the training process.

Data Augmentation Strategy

The data augmentation strategy is designed to enhance the model's robustness and generalization capability by simulating various camera movements and imperfections that might occur in real-world scenarios. This approach ensures the model is well-prepared to handle diverse and unpredictable situations. The augmentation strategy is applied with several considerations to maintain data integrity and ensure realistic training conditions. Augmentations are exclusively applied during the training stage to avoid influencing evaluation results, ensuring that the model's performance is assessed on clean, unaugmented data. Each sequence has a 50% probability of being augmented, which ensures a balanced mix of original and augmented data. This probabilistic approach prevents overfitting to any single type of augmentation. When augmentations are applied, they affect both input and output sequences consistently, maintaining temporal coherence and realism across the sequence, which is crucial for models learning from sequential data. All augmented values are clipped to the range [0, 1], ensuring they remain valid normalized coordinates in the YOLO format. This clipping ensures that the augmented bounding boxes are usable within the model's expected input format. The data loading process also includes error handling mechanisms to manage any inconsistencies in the data, ensuring that training can continue even if individual samples are problematic.

Sequence Reversal

To effectively double the size of the training dataset, reversed sequences are included. For each original sequence $(S_1, S_2, \ldots, S_n)$, a corresponding reversed sequence $(S_n, S_{n-1}, \ldots, S_1)$ is added. This augmentation enables the model to learn to predict both forward and backward camera movements relative to the aircraft refueling port, thereby enhancing its adaptability.

Camera Movement Simulation

Subtle camera movements are simulated to improve the model's robustness to varying camera positions. Panning is applied by introducing a smooth, cumulative random offset to the x and y coordinates of the bounding boxes, simulating the effect of the camera panning horizontally or vertically. The panning effect is modeled as:

$$\text{pan}_t = \sum_{i=1}^{t} \frac{N(0, \sigma^2)}{5}$$

where $N(0, \sigma^2)$ represents a normal distribution with a mean of 0 and variance σ^2. This simulation ensures the model can effectively handle gradual shifts in the camera's viewpoint.

Zoom Simulation

To account for changes in the apparent size of the refueling port due to camera zoom or aircraft movement, a smooth, cumulative scaling factor is applied to the width and height of the bounding boxes. The zoom effect is modeled as:

$$\text{zoom}_t = \prod_{i=1}^{t} U(0.98, 1.02)$$

where $U(0.98, 1.02)$ is a uniform distribution between 0.98 and 1.02. This augmentation prepares the model to adapt to scenarios where the distance between the camera and the refueling port changes dynamically.

Detection Inaccuracy Simulation

To enhance the model's resilience to slight inaccuracies in object detection, small Gaussian noise is added to all bounding box coordinates. This noise is sampled from $N(0, 0.002^2)$ for each coordinate, introducing minor variations that simulate real-world detection imperfections. Such noise mimics the slight inaccuracies that can occur in detection algorithms due to environmental factors or sensor noise.

4.3 Comparison Experiments

To evaluate the performance of the proposed SizPos-GRU model, a series of comparison experiments were conducted using several baseline models. These experiments are designed to assess the model's capability in predicting the future positions and sizes of the refueling port in video sequences. The baseline models considered include the Linear Kalman Filter (LKF), Constant Velocity (CV) model, and variants of Recurrent Neural Networks (RNNs) such as Long Short-Term Memory (LSTM) and Gated Recurrent Unit (GRU).

Linear Kalman Filter (LKF)

The Linear Kalman Filter (LKF) is a recursive filter that estimates the state of a linear dynamic system from a series of incomplete and noisy measurements. In the context of predicting the position of the refueling port, the state vector $\mathbf{x}_t$ includes the position and velocity of the object, while the state transition model assumes constant velocity:

$$\mathbf{x}_t = \mathbf{F}\mathbf{x}_{t-1} + \mathbf{w}_{t-1}, \tag{4.2}$$

$$\mathbf{z}_t = \mathbf{H}\mathbf{x}_t + \mathbf{v}_t, \tag{4.3}$$

where $\mathbf{F}$ is the state transition matrix, $\mathbf{H}$ is the observation matrix, $\mathbf{w}_{t-1}$ is the process noise, and $\mathbf{v}_t$ is the measurement noise. The Kalman filter recursively updates the state estimate $\hat{\mathbf{x}}_t$ and its covariance $\mathbf{P}_t$ through the prediction and update steps:

$$\text{Prediction step:} \quad \hat{\mathbf{x}}_{t|t-1} = \mathbf{F}\hat{\mathbf{x}}_{t-1|t-1}, \tag{4.4}$$

$$\mathbf{P}_{t|t-1} = \mathbf{F}\mathbf{P}_{t-1|t-1}\mathbf{F}^\top + \mathbf{Q}, \tag{4.5}$$

$$\text{Update step:} \quad \mathbf{K}_t = \mathbf{P}_{t|t-1}\mathbf{H}^\top \left(\mathbf{H}\mathbf{P}_{t|t-1}\mathbf{H}^\top + \mathbf{R}\right)^{-1}, \tag{4.6}$$

$$\hat{\mathbf{x}}_{t|t} = \hat{\mathbf{x}}_{t|t-1} + \mathbf{K}_t\left(\mathbf{z}_t - \mathbf{H}\hat{\mathbf{x}}_{t|t-1}\right), \tag{4.7}$$

$$\mathbf{P}_{t|t} = (\mathbf{I} - \mathbf{K}_t\mathbf{H})\,\mathbf{P}_{t|t-1}. \tag{4.8}$$

The Kalman gain $\mathbf{K}_t$ optimally balances the prediction and measurement uncertainties.

Constant Velocity (CV)

The Constant Velocity (CV) model assumes that the object continues to move at a constant speed and direction. Given a sequence of past positions $\mathbf{P} = \{(x_1, y_1), \ldots, (x_T, y_T)\}$, the velocity is estimated as:

$$\mathbf{v} = \frac{1}{T-1}\sum_{t=2}^{T}(\mathbf{P}_t - \mathbf{P}_{t-1}), \tag{4.9}$$

The future positions $\mathbf{F}_k$ for k future steps are predicted by:

$$\mathbf{F}_k = \mathbf{P}_T + k \cdot \mathbf{v}. \tag{4.10}$$

This approach is simple and fast but may be limited in its ability to handle dynamic or non-linear motions.

LSTM Model (PosVelAcc-LSTM)

The PosVelAcc-LSTM model leverages Long Short-Term Memory (LSTM) networks to predict future bounding box positions by encoding past positions, velocities, and accelerations. The architecture includes separate LSTM encoders for each input sequence and decoders for generating the predicted positions and velocities. This model was inspired by the PV-LSTM model from Bouhsain et al. [8].

Algorithm 1 PosVelAcc-LSTM Model

Require: $\mathbf{P}$ (position sequence), $\mathbf{V}$ (velocity sequence), $\mathbf{A}$ (acceleration sequence)
1: Encode past positiosn, velocities, and accelerations using LSTM encoders
2: Combine encoded states: $\mathbf{h}_{\text{combined}} = \mathbf{h}_P + \mathbf{h}_V + \mathbf{h}_A$
3: Initialise decoder inputs with the last observed position and velocity
4: **for** $t = 1$ to k **do** ▷ Predict for k future steps
5: Predict future position: $\hat{\mathbf{P}}_{t+1} = \text{LSTMDecoder}(\mathbf{h}_{\text{combined}})$
6: Predict future velocity: $\hat{\mathbf{V}}_{t+1} = \text{LSTMDecoder}(\mathbf{h}_{\text{combined}})$
7: **end for**
8: **return** Predicted positions and velocities

The model is trained to minimise the smooth L1 loss between predicted and true positions and velocities:

$$\mathscr{L}_{\text{total}} = \text{SmoothL1}(\hat{\mathbf{P}}, \mathbf{P}_{\text{true}}) + \text{SmoothL1}(\hat{\mathbf{V}}, \mathbf{V}_{\text{true}}). \tag{4.11}$$

LSTM Model (SizPos-LSTM)

The SizPos-LSTM model extends the LSTM architecture to predict both the future bounding box positions and sizes. The model architecture includes separate LSTM encoders for the position and size sequences and decoders to predict future positions and sizes.

Algorithm 2 SizPos-LSTM Model

Require: $\mathbf{P}$ (position sequence), $\mathbf{S}$ (size sequence)
1: Encode position and size using LSTM encoders
2: Combine encoded states: $\mathbf{h}_{\text{combined}} = \text{Combine}(\mathbf{h}_P, \mathbf{h}_S)$
3: Initialise decoder inputs with the last observed position and size
4: **for** $t = 1$ to k **do** ▷ Predict for k future steps
5: Predict future position: $\hat{\mathbf{P}}_{t+1} = \text{LSTMDecoder}(\mathbf{h}_{\text{combined}})$
6: Predict future size: $\hat{\mathbf{S}}_{t+1} = \text{LSTMDecoder}(\mathbf{h}_{\text{combined}})$
7: **end for**
8: **return** Predicted positions and sizes

The loss function for training includes terms for both position and size predictions:

$$\mathscr{L}_{\text{total}} = \text{SmoothL1}(\hat{\mathbf{P}}, \mathbf{P}_{\text{true}}) + \text{SmoothL1}(\hat{\mathbf{S}}, \mathbf{S}_{\text{true}}). \tag{4.12}$$

GRU Model (PosVelAcc)

The PosVelAcc-GRU model is similar to the PosVelAcc-LSTM model but uses a Gated Recurrent Unit (GRU) network instead of LSTM for encoding and decoding. GRUs offer computational efficiency while maintaining the ability to capture temporal dependencies. This model was inspired by the Fusion-GRU model from Karim et al. [28].

$$\mathbf{z}_t = \sigma(\mathbf{W}_z \mathbf{x}_t + \mathbf{U}_z \mathbf{h}_{t-1}), \tag{4.13}$$

$$\mathbf{r}_t = \sigma(\mathbf{W}_r \mathbf{x}_t + \mathbf{U}_r \mathbf{h}_{t-1}), \tag{4.14}$$

$$\tilde{\mathbf{h}}_t = \tanh(\mathbf{W}_h \mathbf{x}_t + \mathbf{r}_t \odot \mathbf{U}_h \mathbf{h}_{t-1}), \tag{4.15}$$

$$\mathbf{h}_t = (1 - \mathbf{z}_t) \odot \mathbf{h}_{t-1} + \mathbf{z}_t \odot \tilde{\mathbf{h}}_t, \tag{4.16}$$

where $\mathbf{z}_t$ is the update gate, $\mathbf{r}_t$ is the reset gate, and $\tilde{\mathbf{h}}_t$ is the candidate hidden state.

4.4 Evaluation Metrics

In order to assess the performance of the proposed framework for predicting the future position of aircraft refueling ports, it is imperative to utilise appropriate evaluation metrics that reflect both the accuracy and reliability of the predictions. This section outlines and discusses the four primary evaluation metrics employed in this study: Average Displacement Error (ADE), Final Displacement Error (FDE), Average Intersection over Union (AIoU), and Final Intersection over Union (FIoU). These metrics provide a comprehensive evaluation by measuring different aspects of the predicted trajectories and bounding boxes.

Average Displacement Error (ADE)

The Average Displacement Error (ADE) measures the average Euclidean distance between the predicted bounding box centers and the ground truth bounding box centers over all predicted frames. The ADE provides an overall measure of the spatial accuracy of the prediction model over time. It captures how closely the predicted trajectory follows the actual trajectory of the refueling port. In practical terms, a lower ADE indicates that the model consistently predicts the position of the refueling port with minimal deviation from its true path, which is critical in applications where continuous tracking and precise positioning are essential. It is defined as:

$$\text{ADE} = \frac{1}{m}\sum_{t=1}^{m}\sqrt{(x_t^{\text{pred}} - x_t^{\text{gt}})^2 + (y_t^{\text{pred}} - y_t^{\text{gt}})^2}, \tag{4.17}$$

where m is the number of predicted frames, $(x_t^{\text{pred}}, y_t^{\text{pred}})$ represents the center of the predicted bounding box at the t-th frame, and $(x_t^{\text{gt}}, y_t^{\text{gt}})$ represents the center of the ground truth bounding box at the same frame. x_t^{pred}, y_t^{pred}, x_t^{gt}, y_t^{gt}, and ADE are expressed in pixels.

Final Displacement Error (FDE)

The Final Displacement Error (FDE) focuses on the accuracy of the predicted bounding box center in the final frame of the prediction horizon. The FDE is crucial for evaluating the model's performance at the end of the prediction sequence. It focuses on the model's ability to accurately predict the final position of the refueling port. A lower FDE indicates a high level of precision in predicting the final position. It is defined as the Euclidean distance between the predicted and ground truth bounding box centers at the final frame T:

$$\text{FDE} = \sqrt{(x_T^{\text{pred}} - x_T^{\text{gt}})^2 + (y_T^{\text{pred}} - y_T^{\text{gt}})^2}. \tag{4.18}$$

where $(x_T^{\text{pred}}, y_T^{\text{pred}})$ represents the center of the predicted bounding box at the final frame, and $(x_T^{\text{gt}}, y_T^{\text{gt}})$ represents the center of the ground truth bounding box at the same frame. x_t^{pred}, y_t^{pred}, x_t^{gt}, y_t^{gt}, and ADE are expressed in pixels.

Average Intersection over Union (AIoU)

The Average Intersection over Union (AIoU) evaluates the overlap between the predicted bounding boxes and the ground truth bounding boxes, averaged over all predicted frames. AIoU provides an integrated measure of both the spatial accuracy and the dimensional consistency of the predicted bounding boxes over time. A higher AIoU indicates that the predicted bounding boxes consistently maintain a high degree of overlap with the ground truth, reflecting the model's ability to accurately track both the position and the scale of the refueling port. This metric is particularly relevant in tasks where the object's size and shape are critical, as it ensures that the detected object not only matches the position but also the correct dimensions, which is vital for the subsequent physical interaction with the object. It is computed as:

$$\text{AIoU} = \frac{1}{m}\sum_{t=1}^{m}\frac{A(\mathbf{b}_t^{\text{pred}} \cap \mathbf{b}_t^{\text{gt}})}{A(\mathbf{b}_t^{\text{pred}} \cup \mathbf{b}_t^{\text{gt}})}, \tag{4.19}$$

where $A(\mathbf{b}_t^{\text{pred}} \cap \mathbf{b}_t^{\text{gt}})$ denotes the area of the intersection between the predicted bounding box $\mathbf{b}_t^{\text{pred}}$ and the ground truth bounding box $\mathbf{b}_t^{\text{gt}}$ at the t-th frame, and $A(\mathbf{b}_t^{\text{pred}} \cup \mathbf{b}_t^{\text{gt}})$ denotes the area of their union.

Final Intersection over Union (FIoU)

The Final Intersection over Union (FIoU) assesses the overlap between the predicted bounding box and the ground truth bounding box at the final frame of the prediction horizon. FIoU is a critical metric when the final prediction accuracy is more important than the performance across all frames. It measures how well the predicted bounding box fits the ground truth at the crucial final moment, which is important for tasks that rely on the precise final positioning of an object. For instance, in automated systems that involve docking or alignment tasks, ensuring that the final predicted bounding box is highly accurate in terms of both position and size is essential for successful operation. A higher FIoU score implies a more reliable and accurate final prediction, which is indispensable in high-stakes applications where precision is paramount. It is defined as:

$$\text{FIoU} = \frac{A(\mathbf{b}_T^{\text{pred}} \cap \mathbf{b}_T^{\text{gt}})}{A(\mathbf{b}_T^{\text{pred}} \cup \mathbf{b}_T^{\text{gt}})}, \tag{4.20}$$

where $A(\mathbf{b}_T^{\text{pred}} \cap \mathbf{b}_T^{\text{gt}})$ and $A(\mathbf{b}_T^{\text{pred}} \cup \mathbf{b}_T^{\text{gt}})$ denote the intersection and union areas at the final frame m, respectively.

4.5 Framework Evaluation

This framework integrates YOLOv10 for object detection and a GRU-based model for future position prediction. The process begins by performing object detection across all frames of a video to establish ground truth for each frame. This pre-obtained ground truth simplifies the subsequent evaluation of prediction accuracy. The framework operates in a loop, where it first detects objects in 15 frames, then predicts their positions over the next 30 frames using the GRU model. After each prediction phase, the next 15 frames are analysed for new detections, and this cycle repeats. By having the ground truth available from the outset, the framework allows for efficient evaluation of predictions, directly comparing predicted positions with known ground truth. The following pseudocode outlines the key steps of the framework:

Algorithm 3 Object Detection and Future Position Prediction Framework

procedure RUNFRAMEWORK(*input_video_path*, *yolo_weights_path*, *gru_model_path*, *hparams_file*, *output_video_path*, *output_json_path*, *smoothing_filter*, *lkf*, *input_frames*, *future_frames*)
    Load YOLOv10 model with *yolo_weights_path*
    Open video file at *input_video_path*
    detections ← []
    while frames in video **do**
        frame ← Read next frame
        results ← YOLOv10.detect(*frame*)
        detections ← Extract bounding boxes from *results*
    end while
    Store *detections* as ground truth for all frames
    Initialise loop to process detections in segments
    while more detections to process **do**
        segment_detections ← Take next *input_frames* from *detections*
        track_history_bbox ← Update with *segment_detections*
        if *track_history_bbox* is full **then**
            predicted_positions ← GRU.predict(*track_history_bbox*)
            if *lkf* is True **then**
                predicted_positions ← Apply Kalman Filter to *predicted_positions*
            end if
            smoothed_combined_bboxes ← Apply chosen *smoothing_filter* to *predicted_positions*
            for each future frame in *future_frames* **do**
                Calculate prediction metrics (e.g., ADE, FDE, IoU)
                Annotate frame with current, predicted, and ground-truth bounding boxes
            end for
        end if
        Continue to next *input_frames* in *detections*
    end while
    Save annotated video to *output_video_path*
    Save prediction metrics and smoothed detections to *output_json_path*
end procedure

Chapter 5

Results and Discussion

5.1 Object Detection Training Results

This section presents the final testing results of three different YOLO models (YOLOv10n.pt, YOLOv10s.pt, YOLOv10m.pt) on a dataset involving the classification of fuel port states (CLOSED, SEMI-OPEN, OPEN).

Table 5.1: Performance comparison of YOLO models (YOLOv10n.pt, YOLOv10s.pt, YOLOv10m.pt) on the classification of fuel port states (CLOSED, SEMI-OPEN, OPEN). The table reports Precision (P), Recall (R), mean Average Precision at IoU=0.5 (mAP50), and mean Average Precision across IoU thresholds from 0.5 to 0.95 (mAP50-95) for each state.

Model	Metric	All	Fuel Port [CLOSED]	Fuel Port [SEMI-OPEN]	Fuel Port [OPEN]
YOLOv10n.pt	Precision (P)	0.989	0.994	0.982	0.992
	Recall (R)	0.876	0.657	0.996	0.974
	mAP50	0.893	0.696	0.995	0.987
	mAP50-95	0.852	0.684	0.962	0.909
YOLOv10s.pt	Precision (P)	0.997	0.998	1.000	0.992
	Recall (R)	0.884	0.682	0.997	0.974
	mAP50	0.893	0.694	0.995	0.989
	mAP50-95	0.848	0.678	0.961	0.905
YOLOv10m.pt	Precision (P)	0.994	0.996	0.999	0.988
	Recall (R)	0.888	0.682	1.000	0.983
	mAP50	0.892	0.701	0.995	0.981
	mAP50-95	0.852	0.692	0.968	0.897

Initially, the object detection performance of three YOLO models (YOLOv10n.pt, YOLOv10s.pt, YOLOv10m.pt) was evaluated in detecting the aircraft refueling port under different states: CLOSED, SEMI-OPEN, and OPEN. The performance metrics considered include Precision (P), Recall (R), mean Average Precision (mAP) at different Intersection over Union (IoU) thresholds, and mAP50-95. As summarized in Table 5.1, YOLOv10s.pt achieved the highest precision at 0.997, indicating its superior ability to correctly identify true positives across all classes. In contrast, YOLOv10m.pt demonstrated the highest recall at 0.888, suggesting it was more effective in capturing true positives across various scenarios. Additionally, both YOLOv10n.pt and YOLOv10m.pt yielded the highest mAP50-95 scores at 0.852, reflecting their balanced performance across different IoU thresholds. These results underscore the importance of selecting a model that aligns with specific application requirements. For instance, YOLOv10s.pt may be preferred in environments where precision is paramount, while

YOLOv10m.pt could be more suitable in scenarios demanding higher recall.

5.2 Experiment Results

This section details the outcomes of the experiments conducted to evaluate the performance of various models in predicting the future position of the aircraft refueling port. The analysis covers evaluation metrics, hyperparameter tuning outcomes, and model comparisons, highlighting the effectiveness and robustness of the proposed methods.

5.2.1 Hyperparameter Tuning

Hyperparameter tuning was performed to optimise the performance of the SizPos-GRU model. The experiments evaluated combinations of hidden sizes and hidden depths to determine their impact on Average Displacement Error (ADE), Final Displacement Error (FDE), Average Intersection over Union (AIoU), and Final Intersection over Union (FIoU). As presented in Tables 5.2 and 5.3, the best performance was achieved with a hidden size of 128 and a hidden depth of 8, resulting in an ADE of 32.7 pixels and an FDE of 73.3 pixels when predicting 60 frames into the future using data from the previous 30 frames. This configuration also yielded high AIoU and FIoU scores, indicating a strong overlap with ground truth data. For the scenario involving predictions 30 frames into the future using 15 past frames, a hidden size of 256 and a hidden depth of 8 produced the lowest ADE (17.2 pixels) and FDE (38.6 pixels), with corresponding AIoU and FIoU values that further validate the model's accuracy. These findings highlight the effectiveness of the chosen hyperparameters in enhancing the model's predictive capabilities. The variation in performance across different temporal windows suggests that the model is sensitive to the length of the prediction horizon, which should be considered in future applications.

Table 5.2: Hyperparameter tuning results for trajectory prediction using SizPos-GRU model that leverages 30 past frames (1 sec) to predict the position 60 frames (2 sec) into the future. The table presents the Average Displacement Error (ADE), Final Displacement Error (FDE), Average Intersection over Union (AIoU), and Final Intersection over Union (FIoU) across different configurations of hidden sizes and hidden depths. These metrics help to evaluate the accuracy and spatial consistency of the model's predictions

Hidden Size	Hidden Depth	ADE (pxl)	FDE (pxl)	AIoU (%)	FIoU (%)
32	1	43.3	90.1	39.4	11.5
32	3	44.6	88.5	36.5	13.2
32	6	44.0	79.9	36.9	18.7
32	8	39.2	81.8	40.0	16.1
64	1	53.4	98.6	35.1	13.9
64	3	42.8	87.1	41.2	17.7
64	6	37.0	82.1	44.9	18.5
64	8	35.8	78.8	44.0	18.8
128	1	56.7	96.5	33.3	13.7
128	3	40.9	92.0	43.6	17.5
128	6	32.4	80.9	47.7	16.0
128	**8**	**32.7**	**73.3**	**47.6**	**20.6**
256	1	41.2	86.8	41.5	19.6
256	3	34.0	79.0	47.0	17.5
256	6	35.7	85.0	47.1	17.6
256	8	34.5	82.6	46.2	17.7
512	1	38.3	79.8	44.0	17.3
512	6	35.9	82.7	44.7	18.1
512	8	39.0	81.5	42.5	15.9

Table 5.3: Hyperparameter tuning results for trajectory prediction using SizPos-GRU model that leverages 15 past frames (0.5 sec) to predict the position 30 frames (1 sec) into the future. The table presents the Average Displacement Error (ADE), Final Displacement Error (FDE), Average Intersection over Union (AIoU), and Final Intersection over Union (FIoU) across different configurations of hidden sizes and hidden depths. These metrics help to evaluate the accuracy and spatial consistency of the model's predictions

Hidden Size	Hidden Depth	ADE (pxl)	FDE (pxl)	AIoU (%)	FIoU (%)
32	1	23.0	45.6	58.3	35.9
32	2	23.5	46.3	58.2	34.0
32	4	28.0	59.7	58.5	33.9
32	8	23.3	45.1	56.9	36.3
64	1	29.8	55.2	58.4	35.8
64	2	31.0	56.9	57.1	33.5
64	4	21.2	45.1	61.4	37.4
64	8	20.1	44.1	62.1	39.6
128	1	25.1	48.4	58.6	37.9
128	2	26.6	49.2	50.6	31.4
128	4	25.4	53.6	60.1	33.8
128	8	18.7	42.4	62.5	37.3
256	1	28.0	55.9	58.1	36.5
256	2	22.2	52.0	62.6	35.6
256	4	20.3	50.6	62.8	33.3
256	**8**	**17.2**	**38.6**	**62.4**	**39.4**
512	1	22.8	45.1	58.8	35.3
512	2	27.8	52.0	54.7	34.6
512	4	19.4	43.0	60.2	36.8
512	8	19.3	44.2	60.7	34.0

5.2.2 SizPos-GRU Model Evaluation

The SizPos-GRU model's performance was evaluated against various baseline models in two scenarios: predicting 60 frames into the future using data from the previous 30 frames, and predicting 30 frames into the future using data from the previous 15 frames. The models were assessed based on Average Displacement Error (ADE) and Final Displacement Error (FDE), both in pixels and as a percentage of the maximum possible error, as well as Average Intersection over Union (AIoU) and Final Intersection over Union (FIoU). In the 60-frame prediction task (Table 5.4), the SizPos-GRU model achieved the lowest ADE (34.2 pixels, 4.28%) and FDE (73.4 pixels, 9.18%), demonstrating superior accuracy in predicting future positions. While the FIoU value of 22.1% indicates moderate spatial overlap, the low displacement errors highlight the model's strength in minimising prediction deviations. For the 30-frame prediction task (Table 5.5), the SizPos-GRU model similarly excelled, with an ADE of 17.2 pixels (2.15%) and an FDE of 38.6 pixels (4.83%). Despite the FIoU being a less critical metric in some applications, the low displacement errors confirm the model's reliability in short-term predictions. These results suggest that the SizPos-GRU model is particularly effective in minimising displacement errors, making it a strong candidate for applications where precise trajectory prediction is crucial.

Table 5.4: Performance comparison of various models on trajectory prediction tasks using 30 past frames to predict 60 future frames. The table reports the Average Displacement Error (ADE) and Final Displacement Error (FDE) in both pixels and percentage, as well as Average Intersection over Union (AIoU) and Final Intersection over Union (FIoU). Lower ADE and FDE values indicate better accuracy, while higher AIoU and FIoU values indicate better overlap with ground truth. The SizPos-GRU model demonstrates superior performance across all metrics.

Model	**ADE (pxl)**	**ADE (%)**	**FDE (pxl)**	**FDE (%)**	**AIoU (%)**	**FIoU (%)**
CV	131.5	16.44%	271.0	33.88%	25.4	8.7
LKF	121.1	15.14%	270.3	33.79%	29.3	6.4
PosVelAcc-LSTM (ours)	69.1	8.64%	115.0	14.38%	26.6	11.2
SizPos-LSTM (ours)	49.7	6.21%	95.7	11.96%	41.3	15.7
PosVelAcc-GRU (ours)	81.5	10.19%	121.3	15.16%	23.3	10.7
SizPos-GRU (ours)	**34.2**	**4.28%**	**73.4**	**9.18%**	**46.5**	**22.1**

Table 5.5: Performance comparison of various models on trajectory prediction tasks using 15 past frames to predict 30 future frames. The table reports the Average Displacement Error (ADE) and Final Displacement Error (FDE) in both pixels and percentage, as well as Average Intersection over Union (AIoU) and Final Intersection over Union (FIoU). Lower ADE and FDE values indicate better accuracy, while higher AIoU and FIoU values indicate better overlap with ground truth. The SizPos-GRU model consistently outperforms the other models across all evaluation metrics.

Model	**ADE (pxl)**	**ADE (%)**	**FDE (pxl)**	**FDE (%)**	**AIoU (%)**	**FIoU (%)**
CV	51.7	6.46%	110.2	13.78%	45.2	20.3
LKF	47.7	5.96%	105.8	13.23%	48.6	21.5
PosVelAcc-LSTM (ours)	41.8	5.23%	79.0	9.88%	42.4	20.0
SizPos-LSTM (ours)	25.3	3.16%	49.9	6.24%	58.8	36.1
PosVelAcc-GRU (ours)	39.2	4.90%	77.1	9.64%	46.3	23.1
SizPos-GRU (ours)	**17.2**	**2.15%**	**38.6**	**4.83%**	**62.4**	**39.4**

5.2.3 Framework Evaluation

To thoroughly evaluate the overall performance of the trajectory prediction framework, different smoothing filters and Linear Kalman Filter (LKF) configurations were tested to determine their impact on prediction accuracy. Table 5.6 presents a comprehensive comparison of the results obtained using various smoothing techniques. The analysis reveals that the Savitzky-Golay filter, when used in conjunction with LKF, provided the most accurate predictions. This configuration achieved the lowest Average Displacement Error (ADE) of 32.98 pixels and a Final Displacement Error (FDE) of 57.11 pixels. Additionally, the combination resulted in relatively high Average Intersection over Union (AIoU) and Final Intersection over Union (FIoU) values, indicating better spatial overlap between the predicted and actual positions. These results suggest that the Savitzky-Golay filter, due to its capability to preserve important trajectory trends while filtering out noise, works synergistically with LKF to enhance the predictive performance of the model. In contrast, other smoothing techniques, such as Moving Average and Exponential Smoothing, showed less favorable outcomes. For instance, the Moving Average

filter, despite being effective in some scenarios, led to significantly higher FDE values, reflecting a lag effect in the predictions, particularly in dynamic environments. Exponential Smoothing, while slightly better, still did not match the performance of the Savitzky-Golay filter in terms of overall accuracy. Table 5.7 extends the evaluation to different video datasets, further illustrating the framework's performance across varied test scenarios. While the Savitzky-Golay filter with LKF configuration continued to outperform other setups in certain videos, such as *video_lab_platform_6*, the results across other datasets, like *test_indoor1*, showed a noticeable decline in predictive accuracy, with ADE and FDE values increasing significantly. This variance underscores the importance of considering the specific characteristics of the application environment when choosing the appropriate smoothing and filtering techniques.

Table 5.6: Performance metrics using different smoothing filters and Linear Kalman Filter (LKF) configurations for the video *video_lab_platform_6*. The table presents Average Displacement Error (ADE), Final Displacement Error (FDE), Average Intersection over Union (AIoU), and Final Intersection over Union (FIoU). The results demonstrate the impact of various filtering techniques on the model's predictive accuracy.

Smooth Filter	**LKF**	**ADE (px)**	**ADE (%)**	**FDE (px)**	**FDE (%)**	**AIoU (%)**	**FIoU (%)**
Savitzky-Golay (sa)	**True**	**32.98**	**4.12**	**57.11**	**7.14**	**49.16**	**33.67**
Moving Average (ma)	True	36.95	4.62	151.76	18.97	47.42	0.27
Exponential Smoothing (es)	True	37.05	4.63	57.61	7.20	43.81	32.86
Hybrid	True	35.31	4.41	126.92	15.86	48.15	2.42
Adaptive	True	33.33	4.17	57.66	7.21	48.48	32.90
No Smoothing	True	33.33	4.17	57.66	7.21	48.48	32.90
Savitzky-Golay (sa)	False	32.47	4.06	60.58	7.57	49.69	31.55
Moving Average (ma)	False	36.06	4.51	148.99	18.62	48.19	0.46
Exponential Smoothing (es)	False	36.98	4.62	59.49	7.44	43.10	32.30
Hybrid	False	34.61	4.33	124.50	15.56	48.72	2.88
Adaptive	False	32.53	4.07	60.58	7.57	49.63	31.90
No Smoothing	False	32.53	4.07	60.58	7.57	49.63	31.90

Table 5.7: Framework Test with LKF and Savitzky-Golay filter for the videos *video_lab_platform_6*, *test_indoor1*, and *video_lab_semiopen_1_____3*. The table presents Average Displacement Error (ADE), Final Displacement Error (FDE), Average Intersection over Union (AIoU), and Final Intersection over Union (FIoU) for each video. The results demonstrate the model's predictive accuracy across different scenarios.

Video	**ADE (px)**	**ADE (%)**	**FDE (px)**	**FDE (%)**	**AIoU (%)**	**FIoU (%)**
video_lab_platform_6	**32.98**	**4.12**	**57.11**	**7.14**	**49.16**	**33.67**
test_indoor1	97.10	12.14	125.35	15.67	21.92	11.41
video_lab_semiopen_1_____3	79.50	9.94	124.75	15.59	18.09	4.57

5.3 Testing Visualisation

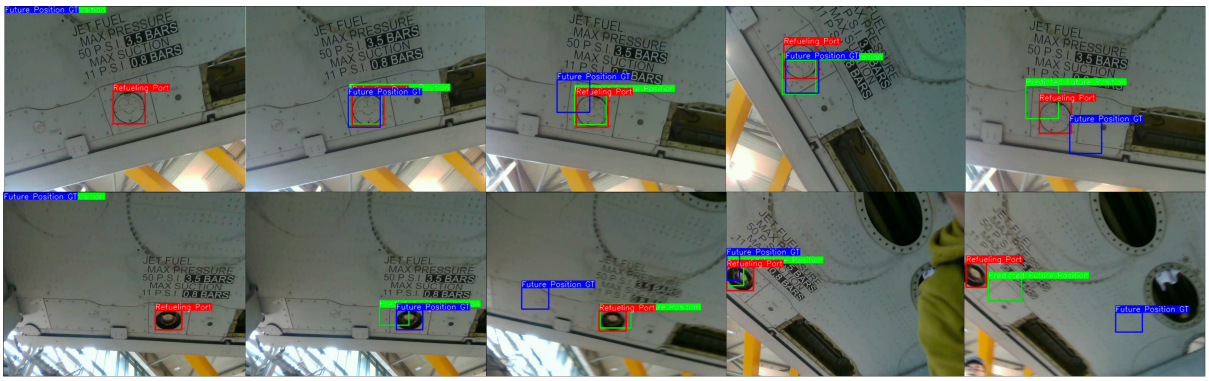

Figure 5.1: Visualisation of the trajectory prediction framework output for the *video_lab_platform_6* and *test_indoor1* videos. The figure shows the ground truth trajectory (blue) and the predicted trajectory (red) for the refueling port. The close alignment between the predicted and actual trajectories demonstrates the model's accuracy in predicting the object's future positions.

This section provides a detailed analysis of the trajectory prediction framework's performance using two distinct video datasets: *video_lab_platform_6* and *test_indoor1*. The figures illustrate the predicted and ground truth central positions of the refueling port across various sequences of frames. The analysis compares the results obtained without smoothing (raw data) and with the application of the Savitzky-Golay filter combined with a Linear Kalman Filter (LKF), highlighting the impact of these smoothing techniques on prediction accuracy. Figure 5.1 presents an initial visualization of the trajectory prediction framework's output. In both the *video_lab_platform_6* and *test_indoor1* datasets, the predicted trajectory (red) closely follows the ground truth trajectory (blue). This visual alignment indicates that the model is generally effective in predicting the object's future positions, demonstrating its robustness across different video scenarios. In Figure 5.2, the predicted and ground truth central positions are plotted for the *video_lab_platform_6* dataset without any smoothing applied. The results show that the model's predictions initially align with the ground truth; however, as the frames progress, particularly in the later sequences (frames 151 to 180), the deviations become more pronounced. This suggests that the model's raw predictions are sensitive to noise and may accumulate errors over time, leading to a drift from the actual trajectory. The application of the Savitzky-Golay filter combined with LKF, as shown in Figure 5.3, significantly improves the prediction accuracy for the same dataset. The smoothed predictions exhibit a closer alignment with the ground truth across all frame sequences. The filter effectively reduces the fluctuations and erratic deviations observed in the raw predictions, particularly in the later sequences where the model previously struggled. The smoothed data indicates that the filters help the model maintain stability and accuracy over extended sequences, mitigating the effects of cumulative prediction errors. Figure 5.4 depicts the performance of the model on the *test_indoor1* dataset without smoothing. The model's predictions show significant deviations from the ground truth, especially in the final sequence of frames (196 to 225), where abrupt changes in the trajectory are not well captured by the model. The lack of smoothing results in predictions that are highly sensitive to noise, leading to large prediction errors and a noticeable drift from the actual trajectory. In contrast, Figure 5.5 shows the predictions for the *test_indoor1* dataset with the Savitzky-Golay filter and LKF applied. The filtered predictions demonstrate a marked improvement in accuracy, with

the trajectories closely following the ground truth across all frame sequences. The smoothing techniques significantly reduce the impact of noise and sudden changes in the object's movement, resulting in more reliable and consistent predictions. The final sequence, which previously showed large deviations, now exhibits a stable and accurate trajectory, underscoring the effectiveness of the filtering approach in enhancing the model's performance. Overall, the comparison between the unsmoothed and smoothed data highlights the importance of applying smoothing techniques in trajectory prediction tasks. The raw predictions, while initially accurate, tend to degrade over time due to noise and error accumulation. However, the application of the Savitzky-Golay filter and LKF successfully mitigates these issues, providing a stable and accurate prediction across different video scenarios. These findings emphasize the necessity of such techniques in real-world applications where data variability and noise are common, ensuring that the model can reliably predict future positions with high precision.

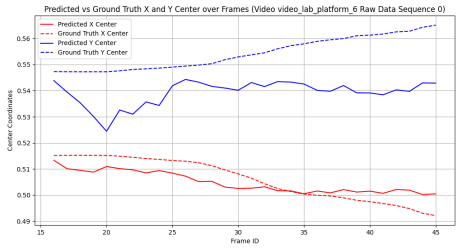

(a) Predictions from frame 16 to 45.

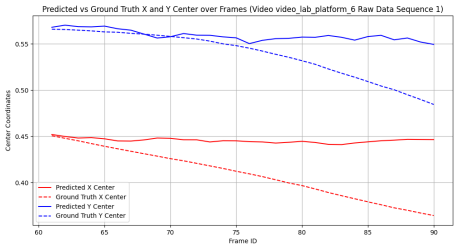

(b) Predictions from frame 61 to 90.

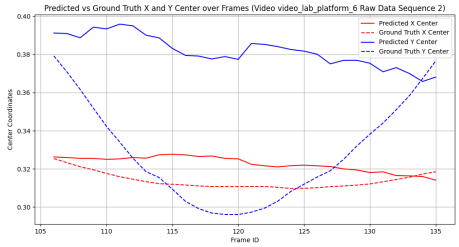

(c) Predictions from frame 106 to 135.

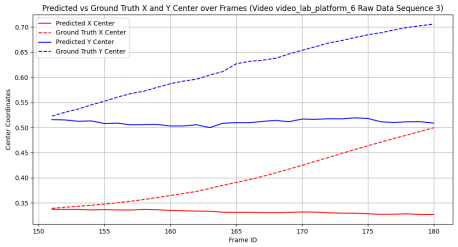

(d) Predictions from frame 151 to 180.

Figure 5.2: Predicted vs Ground Truth Central Position for video *video_lab_platform_6* (No Smoothing).

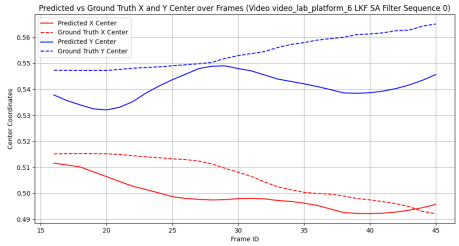

(a) Predictions from frame 16 to 45.

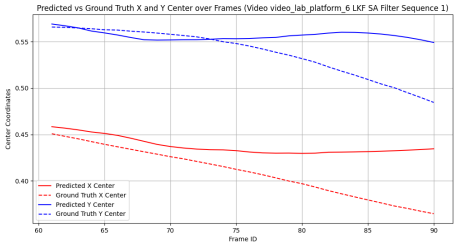

(b) Predictions from frame 61 to 90.

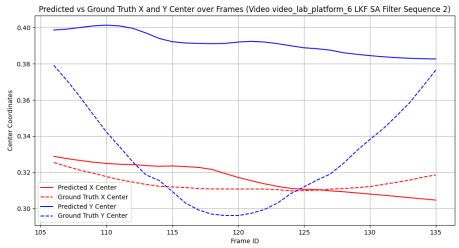

(c) Predictions from frame 106 to 135.

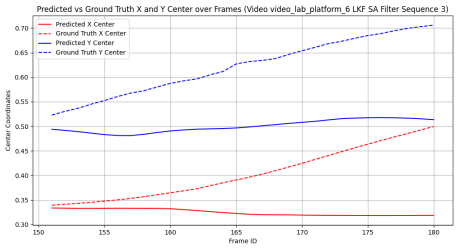

(d) Predictions from frame 151 to 180.

Figure 5.3: Predicted vs Ground Truth Central Position for video *video_lab_platform_6* (Savitzky-Golay & LKF filter).

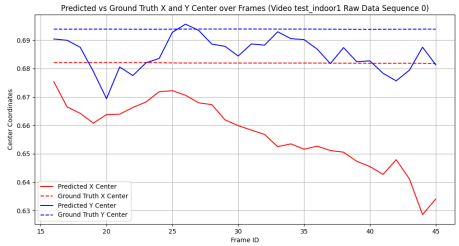

(a) Predictions from frame 16 to 45.

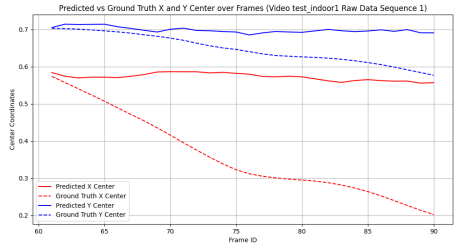

(b) Predictions from frame 61 to 90.

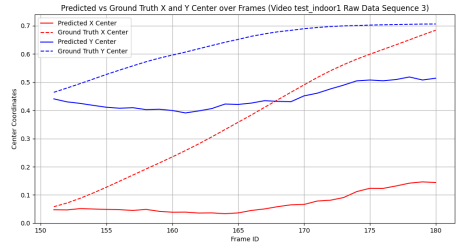

(c) Predictions from frame 151 to 180.

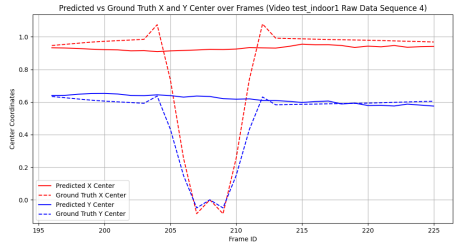

(d) Predictions from frame 196 to 225.

Figure 5.4: Predicted vs Ground Truth Central Position for video *test_indoor1* (No Smoothing).

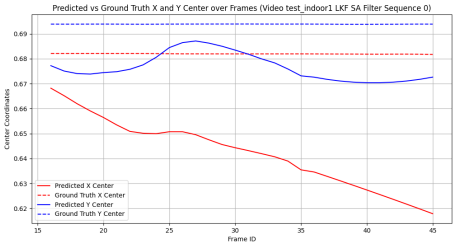

(a) Predictions from frame 16 to 45.

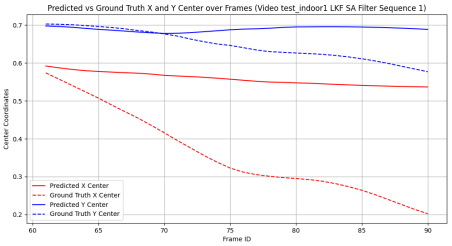

(b) Predictions from frame 61 to 90.

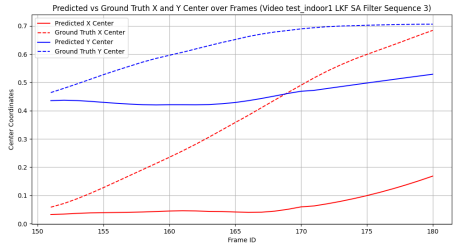

(c) Predictions from frame 151 to 180.

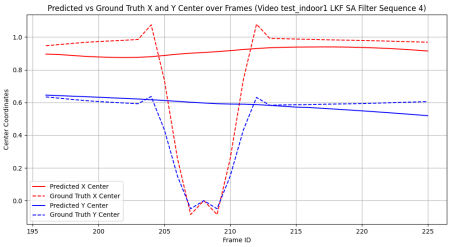

(d) Predictions from frame 196 to 225.

Figure 5.5: Predicted vs Ground Truth Central Position for video *test_indoor1* (Savitzky-Golay & LKF filter).

Chapter 6

Conclusion and Future Work

References

1. A. Alahi, K. Goel, V. Ramanathan, A. Robicquet, L. Fei-Fei, and S. Savarese. Social lstm: Human trajectory prediction in crowded spaces. volume 2016-December, 2016. doi: 10.1109/CVPR.2016.110.

2. J. Ansel, E. Yang, H. He, N. Gimelshein, A. Jain, M. Voznesensky, B. Bao, P. Bell, D. Berard, E. Burovski, G. Chauhan, A. Chourdia, W. Constable, A. Desmaison, Z. DeVito, E. Ellison, W. Feng, J. Gong, M. Gschwind, B. Hirsh, S. Huang, K. Kalambarkar, L. Kirsch, M. Lazos, M. Lezcano, Y. Liang, J. Liang, Y. Lu, C. Luk, B. Maher, Y. Pan, C. Puhrsch, M. Reso, M. Saroufim, M. Y. Siraichi, H. Suk, M. Suo, P. Tillet, E. Wang, X. Wang, W. Wen, S. Zhang, X. Zhao, K. Zhou, R. Zou, A. Mathews, G. Chanan, P. Wu, and S. Chintala. PyTorch 2: Faster Machine Learning Through Dynamic Python Bytecode Transformation and Graph Compilation. In *29th ACM International Conference on Architectural Support for Programming Languages and Operating Systems, Volume 2 (ASPLOS '24)*. ACM, Apr. 2024. doi: 10.1145/3620665.3640366. URL https://pytorch.org/assets/pytorch2-2.pdf.

3. A. F. C. A. C. A. . M. C. (AvMC). Ar3p program background (2017-2019) and robotic hot refueling demonstrations (sep-oct 2020), 2020. URL hhttps://www.denix.osd.mil/ndcee/denix-files/sites/44/2023/09/EXSUM-AR3P-Robotic-Refueling-K-MAX-and-S-70-Sep_Oct-2020-v9.pdf. Accessed: 2024-06-24.

4. J. Bailey. What is fuel tankering and why should you care?, 2019. URL https://simpleflying.com/fuel-tankering/. Accessed: 2024-06-24.

5. R. A. Bennett, Y. C. Shiu, and M. B. Leahy. A robust light invariant vision system for aircraft refueling. volume 1, 1991. doi: 10.1109/robot.1991.131568.

6. S. Blakey, L. Rye, and C. W. Wilson. Aviation gas turbine alternative fuels: a review. *Proceedings of the Combustion Institute*, 33(2):2863–2885, 2011. doi: 10.1016/j.proci.2010.09.011.

7. A. Bochkovskiy, C. Wang, and H. M. Liao. Yolov4: Optimal speed and accuracy of object detection. *CoRR*, abs/2004.10934, 2020. URL https://arxiv.org/abs/2004.10934.

8. S. A. Bouhsain, S. Saadatnejad, and A. Alahi. Pedestrian intention prediction: A multi-task perspective. *CoRR*, abs/2010.10270, 2020. URL https://arxiv.org/abs/2010.10270.

9. H. Burnette. Lab demonstrates robotic ground refueling of aircraft, Oct. 2010. URL https://www.wpafb.af.mil/News/Article-Display/Article/400022/lab-demonstrates-robotic-ground-refueling-of-aircraft/. Accessed: 2024-06-24.

10. F. Chen, X. Wang, Y. Zhao, S. Lv, and X. Niu. Visual object tracking: A survey. *Computer Vision and Image Understanding*, 222, 9 2022. ISSN 1090235X. doi: 10.1016/j.cviu.2022.103508.

11. Y. Chen, X. Yuan, R. Wu, J. Wang, Q. Hou, and M.-M. Cheng. Yolo-ms: Rethinking multi-scale representation learning for real-time object detection, 2023.

12. G. Cheng, X. Yuan, X. Yao, K. Yan, Q. Zeng, X. Xie, and J. Han. Towards large-scale small object detection: Survey and benchmarks. *IEEE Transactions on Pattern Analysis and Machine Intelligence*, 45, 2023. ISSN 19393539. doi: 10.1109/TPAMI.2023.3290594.

13. O. Cokorilo, S. Gvozdenovic, L. Vasov, and P. Mirosavljevic. Costs of unsafety in aviation. *Technological and Economic Development of Economy - TECHNOL ECON DEV ECON*, 16:188–201, 06 2010. doi: 10.3846/tede.2010.12.

14. J. Dai, Y. Li, K. He, and J. Sun. R-FCN: object detection via region-based fully convolutional networks. *CoRR*, abs/1605.06409, 2016. URL http://arxiv.org/abs/1605.06409.

15. H. Face. Object detection leaderboard, 2023. URL https://huggingface.co/blog/object-detection-leaderboard. Accessed: 2024-06-17.

16. W. Falcon and The PyTorch Lightning team. PyTorch Lightning, Mar. 2019. URL https://github.com/Lightning-AI/lightning.

17. N. Ficken. Concept demonstration explores robotic aviation refueling system, July 18 2017. URL https://www.army.mil/article/190980/concept_demonstration_explores_robotic_aviation_refueling_system. Accessed: 2024-06-24.

18. Z. Ge, S. Liu, F. Wang, Z. Li, and J. Sun. YOLOX: exceeding YOLO series in 2021. *CoRR*, abs/2107.08430, 2021. URL https://arxiv.org/abs/2107.08430.

19. A. Ghosh. Yolov10: The dual-head og of yolo series, 2024. URL https://learnopencv.com/yolov10/. Accessed: 2024-06-24.

20. R. B. Girshick. Fast R-CNN. *CoRR*, abs/1504.08083, 2015. URL http://arxiv.org/abs/1504.08083.

21. R. B. Girshick, J. Donahue, T. Darrell, and J. Malik. Rich feature hierarchies for accurate object detection and semantic segmentation. *CoRR*, abs/1311.2524, 2013. URL http://arxiv.org/abs/1311.2524.

22. K. Gong, B. Liu, X. Xu, Y. Xu, Y. He, Z. Zhang, and J. Rasol. Research of an unmanned aerial vehicle autonomous aerial refueling docking method based on binocular vision. *Drones*, 7, 2023. ISSN 2504446X. doi: 10.3390/drones7070433.

23. Intel. Intel realsense depth camera d435, 2024. URL https://www.intelrealsense.com/depth-camera-d435/. Accessed: 2024-06-24.

24. G. Jocher. Yolov5 release v7.0, 2022. URL https://github.com/ultralytics/yolov5/tree/v7.0.

25. G. Jocher. Yolov8, 2023. URL https://github.com/ultralytics/ultralytics/tree/main.

26. G. Jocher, A. Chaurasia, and J. Qiu. Ultralytics YOLO, Jan. 2023. URL https://github.com/ultralytics/ultralytics.

27. J. Kang, S. Tariq, H. Oh, and S. Woo. A survey of deep learning-based object detection methods and datasets for overhead imagery. *IEEE Access*, 10:1–1, 01 2022. doi: 10.1109/ACCESS.2022.3149052.

28. M. M. Karim, R. Qin, and Y. Wang. Fusion-gru: A deep learning model for future bounding box prediction of traffic agents in risky driving videos. *Transportation Research Record*, 2024. ISSN 21694052. doi: 10.1177/03611981241230540.

29. B. Kuang, S. Barnes, G. Tang, and K. Jenkins. A dataset for autonomous aircraft refueling on the ground (agr). 2023. doi: 10.1109/ICAC57885.2023.10275212.

30. J. Kugarajeevan, T. Kokul, A. Ramanan, and S. Fernando. Transformers in single object tracking: An experimental survey. *IEEE Access*, 11, 2023. ISSN 21693536. doi: 10.1109/ACCESS.2023.3298440.

31. W. C. Lee, Y. B. Jeon, S. S. Han, and C. S. Jeong. Position prediction in space system for vehicles using artificial intelligence. *Symmetry*, 14, 2022. ISSN 20738994. doi: 10.3390/sym14061151.

32. C. Li, L. Li, Y. Geng, H. Jiang, M. Cheng, B. Zhang, Z. Ke, X. Xu, and X. Chu. Yolov6 v3.0: A full-scale reloading, 2023.

33. T.-Y. Lin, P. Goyal, R. Girshick, K. He, and P. Dollár. Focal loss for dense object detection, 2018.

34. K. Liu, L. Chen, and X. Liu. Research on application of frontier technologies at smart airport. In J. Zeng, P. Qin, W. Jing, X. Song, and Z. Lu, editors, *Data Science*, pages 319–330, Singapore, 2021. Springer Singapore. ISBN 978-981-16-5943-0.

35. S. Liu, D. Liu, G. Srivastava, D. Połap, and M. Woźniak. Overview and methods of correlation filter algorithms in object tracking. *Complex and Intelligent Systems*, 7, 2021. ISSN 21986053. doi: 10.1007/s40747-020-00161-4.

36. W. Liu, D. Anguelov, D. Erhan, C. Szegedy, S. E. Reed, C. Fu, and A. C. Berg. SSD: single shot multibox detector. *CoRR*, abs/1512.02325, 2015. URL http://arxiv.org/abs/1512.02325.

37. M. D. L. Olja Čokorilo and G. Dell'Acqua. Aircraft safety analysis using clustering algorithms. *Journal of Risk Research*, 17(10):1325–1340, 2014. doi: 10.1080/13669877.2013.879493. URL https://doi.org/10.1080/13669877.2013.879493.

38. E. Plaza and M. Santos. Knowledge based approach to ground refuelling optimization of commercial airplanes. *Expert Systems*, 38, 2021. ISSN 14680394. doi: 10.1111/exsy.12631.

39. J. Redmon and A. Farhadi. YOLO9000: better, faster, stronger. *CoRR*, abs/1612.08242, 2016. URL http://arxiv.org/abs/1612.08242.

40. J. Redmon, S. K. Divvala, R. B. Girshick, and A. Farhadi. You only look once: Unified, real-time object detection. *CoRR*, abs/1506.02640, 2015. URL http://arxiv.org/abs/1506.02640.

41. S. Ren, K. He, R. Girshick, and J. Sun. Faster r-cnn: Towards real-time object detection with region proposal networks. *IEEE Transactions on Pattern Analysis and Machine Intelligence*, 39, 2017. ISSN 01628828. doi: 10.1109/TPAMI.2016.2577031.

42. R. Sati, S. Singh, and R. Yadav. Aircraft fuel system: design, components, and safety. *International Journal of Aerospace Engineering*, 2019:1–12, 2019. doi: 10.1155/2019/6943787.

43. E. R. Schultz. Robotic systems for aircraft servicing/maintenance. *IEEE Aerospace and Electronic Systems Magazine*, 1, 1986. ISSN 08858985. doi: 10.1109/MAES.1986.5005018.

44. O. Styles, T. Guha, and V. Sanchez. Multiple object forecasting: Predicting future object locations in diverse environments. 2020. doi: 10.1109/WACV45572.2020.9093446.

45. A. Wang, H. Chen, L. Liu, K. Chen, Z. Lin, J. Han, and G. Ding. Yolov10: Real-time end-to-end object detection, 2024.

46. C. Wang, W. He, Y. Nie, J. Guo, C. Liu, K. Han, and Y. Wang. Gold-yolo: Efficient object detector via gather-and-distribute mechanism, 2023.

47. C.-Y. Wang, I.-H. Yeh, and H.-Y. M. Liao. Yolov9: Learning what you want to learn using programmable gradient information, 2024.

48. X. Wang, X. Dong, X. Kong, J. Li, and B. Zhang. Drogue detection for autonomous aerial refueling based on convolutional neural networks. *Chinese Journal of Aeronautics*, 30, 2017. ISSN 10009361. doi: 10.1016/j.cja.2016.12.022.

49. J. Wu and S. Xu. From point to region: Accurate and efficient hierarchical small object detection in low-resolution remote sensing images. *Remote Sensing*, 13, 2021. ISSN 20724292. doi: 10.3390/rs13132620.

50. S. Xu, X. Wang, W. Lv, Q. Chang, C. Cui, K. Deng, G. Wang, Q. Dang, S. Wei, Y. Du, and B. Lai. Pp-yoloe: An evolved version of yolo, 2022.

51. X. Xu, Y. Jiang, W. Chen, Y. Huang, Y. Zhang, and X. Sun. Damo-yolo : A report on real-time object detection design, 2023.

52. T. Ye, W. Qin, Z. Zhao, X. Gao, X. Deng, and Y. Ouyang. Real-time object detection network in uav-vision based on cnn and transformer. *IEEE Transactions on Instrumentation and Measurement*, 72, 2023. ISSN 15579662. doi: 10.1109/TIM.2023.3241825.

53. S. Yildirim, Z. Rana, and G. Tang. Autonomous ground refuelling approach for civil aircrafts using computer vision and robotics. volume 2021-October, 2021. doi: 10.1109/DASC52595.2021.9594312.

54. S. Yildirim, Z. A. Rana, and G. Tang. Development of vision guided real-time trajectory planning system for autonomous ground refuelling operations using hybrid dataset. 2023. doi: 10.2514/6.2023-1148.

55. S. S. A. Zaidi, M. S. Ansari, A. Aslam, N. Kanwal, M. Asghar, and B. Lee. A survey of modern deep learning based object detection models, 2022. ISSN 10512004.

56. Y. Zhang, T. Wang, K. Liu, B. Zhang, and L. Chen. Recent advances of single-object tracking methods: A brief survey. *Neurocomputing*, 455, 2021. ISSN 18728286. doi: 10.1016/j.neucom.2021.05.011.

57. Z. Zhong, D. Li, H. Wang, and Z. Su. Drogue position and tracking with machine vision for autonomous air refueling based on ekf. volume 2, 2017. doi: 10.1109/IHMSC.2017.151.